Jonas Nygård

Numerical investigation of 3D flow around a circular cylinder with forced oscillations

Master's thesis in Marine Technology
Supervisor: Professor Lars Erik Holmedal, NTNU
Co-supervisor: Fengjian Jiang, Sintef Ocean
June 2023

◻ NTNU
Norwegian University of
Science and Technology

Jonas Nygård

Numerical investigation of 3D flow around a circular cylinder with forced oscillations

Master's thesis in Marine Technology
Supervisor: Professor Lars Erik Holmedal, NTNU
Co-supervisor: Fengjian Jiang, Sintef Ocean
June 2023

Norwegian University of Science and Technology
Faculty of Engineering
Department of Marine Technology

NTNU
Norwegian University of
Science and Technology

Preface

This report summarizes the work conducted for the Master's thesis in Marine Hydrodynamics at NTNU, Trondheim. The thesis was completed independently in the spring of 2023.

The scope of the work has been to do a Computational Fluid Dynamics simulation of the viscous flow around a circular cylinder for Reynolds number 24000. The aim of the thesis was to develop an engineering method based on Computational Fluid Dynamics, to model the fluid-structure interaction of a three-dimensional oscillating cylinder and to compare the results with the experiments done here at Marintek by K.H. Aronsen.

Much work was spent during the semester on the preprocessing portion of the analysis. Trying to get the grid to work in order to produce the most accurate findings was a very difficult portion of the thesis. This was unsuccessful as the grid never worked properly and the time it took trying to fix it made it impossible to try another one because of time issues. Anyway, the work was meaningful as I learned a lot about Computational Fluid Dynamics and Vortex Induced Vibrations. This, I will bring with me regardless of the results turning out the way they did. The Betzy supercomputer was used to execute the simulations.

Abstract

Circular cylinders are utilized in a variety of marine applications such as pipelines and risers. Several experiments done at Marintek was conducted by K.H. Aronsen on the problem of a cylinder oscillating in both x and y-direction. The problem of this thesis is to find an engineering method to numerically replicate these findings.

Large Eddy Simulation (LES) with a Smagorinsky subgrid scale model is used to numerically simulate turbulent 3D flow around a forced oscillating cylinder. The Reynolds number is 24000, which is in the subcritical flow domain, based on a cylinder diameter of 0.1 meters and a free stream velocity of U = 0.24 m/s. The code used is the commercial software STAR-CCM+

The cylinder is forced to oscillate in both x and y-direction and a structured mesh with a prism layer is made for two geometries and different mesh sizes to look at convergence. The results are presented as; hydrodynamic coefficients, vorticity distribution and motion plots. The results are compared to published experimental findings. The main findings are that the chosen mesh time is not working to solve the problem at hand and that a new mesh type or a finer mesh must be used.

Further work can be to use the existing mesh but refine it to run longer and heavier simulations, try the mesh on a simpler problem or try a different mesh type.

Sammendrag

Sirkulære sylindere blir brukt i ulike maritime anvendelser som rørledninger og stigerør. Flere eksperimenter utført ved Marintek ble gjennomført av K.H. Aronsen på problemet med en sylinder som svinger både i x- og y-retning. Problemstillingen i denne avhandlingen er å finne en ingeniørmetode for å kunne gjenskape disse funnene numerisk.

Large Eddy Simulations med en Smagorinsky subgrid scale modell blir brukt for å numerisk simulere den turbulente tre-dimensjonale strømningen rundt en tvungen svingende sylinder. Reynoldstallet er 24000, noe som ligger i det subkritiske strømningsspekteret, basert på en sylinderdiameter på 0,1 meter og en strømhastighet på U = 0,24 m/s. Koden som blir brukt er den kommersielle programvaren STAR-CCM+.

Sylinderen blir tvunget til å svinge både i x- og y-retning, og et strukturert mesh med et "prismlayer" er blitt laget for to geometrier og tre ulike meshstørrelser for å undersøke konvergens. Resultatene blir presentert som hydrodynamiske koeffisienter, vortisitetsfordeling og plottet bevegelse. Resultatene blir sammenlignet med publiserte eksperimentelle funn. De viktigste funnene er at det valgte meshet ikke fungerer til å løse problemet som blir studert, og at en ny meshtype eller et finere mesh må brukes.

Videre arbeid kan være å bruke det eksisterende meshet, men forbedre det for så å kjøre lengre og tyngre simuleringer, eller å prøve meshet på et enklere problem eller prøve en annen meshtype.

Table of Contents

Abbreviations

ALE	Arbitrary Langrangian-Eulerian
BM	Boundary layer
CF	Cross-flow direction
CFD	Computational Fluid Dynamics
DES	Detached Eddy Simulation
DNS	Direct Numerical Simulation
DNV	Det Norske Veritas
$FPSO$	Floating Production Storage and Offloading
IBM	Immersed Boundary Method
IL	In-line direction
LES	Large Eddy Simulation
$N-S$	Navier-Stokes
$RANS$	Reynolds Averaged Navier Stokes
RMS	Root Mean Square
VIM	Vortex Induced Motions
VIV	Vortex Induced Vibrations

Symbols

δ delta

t time

z vertical coordinate, positive upwards

u fluid particle velocity

U velocity of fluid

L characteristic length

ν kinematic viscosity

D diameter

Re Reynolds number

St Strouhal number

f_v vortex shedding frequency

F_D drag force

F_L lift force

C_L lift coefficient

C_D drag coefficient

A_L lift ampitude

A_D drag amplitude

f_n natural frequency

U_R reduced velocity

∂ partial derivate

$\tilde{u}_i$ instantaneous value

U_i mean part of instantaneous velocity

u_i fluctuating part of instantaneous value

ρ water density

g acceleration of gravity

F force

ϵ epsilon

ω omega

f_S shedding frequency of S-cell vortex

f_N shedding frequency of N-cell vortex

f_L shedding frequency of L-cell vortex

λ lambda

List of Figures

List of Tables

1 Introduction

New deep-water oil and gas resources have been found in recent years in places that have particularly irregular seabed characteristics, and this trend is expected to persist in the years to come. Pipeline installation in such places is likely to result in an extensive amount of free spans. Ocean currents will cause divided flow and vortex shedding here and these vortices will once again exert stresses on the pipe, potentially resulting in horizontal and vertical oscillations. This phenomenon is referred to as vortex induced vibrations (VIV), and the horizontal and vertical oscillations are referred to as in-line (IL) and cross-flow (CF), respectively. These oscillations cause time-varying stresses in the pipe, resulting in an accumulation of fatigue damage [20].

1.1 Scope of Work

The overall goal of this thesis is to develop an engineering method based on Computational Fluid Dynamics, to model the fluid-structure interaction of a three-dimensional forced oscillating cylinder and to compare the results with the experiments by Aronsen [4].

To determine the scope of study for this thesis, the following objectives are established:

- Get to know basic theory and previous work done on Vortex Induced Vibrations (VIV) and flow over cylinders.

- Learn to use the commercial code STAR-CCM+

- Present results from simulations and discuss the validity of them.

- Create a solid foundation for future research on the subject.

- Come up with suggestions on further work on the problem.

1.2 Literature Review

For several decades, vortex induced vibration of slender marine structures has been the focus of substantial studies. Offshore risers have received a lot of attention in the studies. Risers can be thought of as indefinitely long structures as the boundary conditions are unimportant. Free spanning pipelines, on the other hand, are distinguished by:

- Short spans, i.e. the boundary conditions, become critical for the span's dynamics.

- Proximity to the seafloor. This may affect the inflow conditions and, for significant oscillations, may result in nonlinear responses due to seafloor interactions.

- Multiple varieties of configurations.

- Dynamic interaction with neighboring spans, known as multi-span.

- Damping at the span shoulders as a result of pipe-soil interaction.

Vortex-induced vibrations can be thought of as a self-excited and self-limited response, with the maximum amplitude determined through the complex relationship between the oscillating structure and the fluid. The hydrodynamic forces are generally divided into two categories: additional mass and force in phase with the local response velocity, which indicates energy transfer between the fluid and the structure. In the interest of pure cross-flow VIV some studies have been conducted by Triantafyllou et al. [42] and Carberry et al. [10] in the interest of forced motion. For free vibrations in CF direction, Govardhan and Williamson [22], Vikestad [45] and Jauvtis and Williamson [27] have conducted studies.

In recent years, there has been a greater emphasis on two degree of freedom motions, namely the combination of IL and CF response. There were two reasons for looking into this. To begin, it has been discovered that IL motion influence CF response and alter response amplitudes in addition to conditions for the initiation of VIV. Second, IL oscillations are significant in and of themselves because of three effects [6].

- The IL response will occur at a frequency that is double that of the CF response, resulting in a greater number of stress cycles than the CF response.

- A flexible beam's IL response will often begin at a lower velocity of flow than CF. As a result, IL motions may considerably contribute to fatigue building during long durations of low current velocity.

- Active modeshapes for IL response are often higher order than CF modeshapes. As a result, even though the amplitude is lower, IL dynamic stresses due to bending may become greater than CF.

These findings have heightened interest in pure IL VIV and simultaneous responses in the two directions. Aronsen [4] discovered hydrodynamic coefficients for pure IL oscillations, which is especially useful for free spanning pipelines, while research by Moe and Wu [31], Sarpkaya [38] and Jeon and Gharib [28], provide vital insight into the combined response type.

Aronsen [4] recently investigated the fluid forces on a rigid circular cylinder using a series of 2 Degree of Freedom (DOF) forced oscillation experiments. One of the published discoveries is that when the oscillation patterns have the same shape but opposite orbital direction, the fluid force in phase with the response velocity may have the opposite sign and magnitude. The standard 2C and 2T vortex shedding

modes seen in the studies by Williamson and Jauvtis [27] are also observed during the 2 DOF testing. The drag force and higher order harmonic forces have also been identified and utilized to investigate the interaction of IL and CF motions.

With the rapid advancement in computation efficiency and data storage capacity, an alternative to experiments as the sole method of resolving VIV problems has emerged: Computational Fluid Dynamics (CFD). Blackburn et al [8] and Anagnosto-poulos et al [2], are credited with pioneering numerical research on cylinder VIV. Huang [48] investigated the 2 DOF motion of a circular cylinder in horizontal shear flow. In the 2D RANS simulations, a shear ratio lock-in zone and a new motion trace known as the water-drop shape were discovered. Tutar and Holdo [44] and Al-Jamal and Dalton [26] have also reported 3D LES analysis of VIV. This research concluded that 3-D LES analysis can provide more accurate flow field estimates and hydrodynamic force coefficients than 2D RANS approaches.

1.3 Previous Work - Project Thesis

This master thesis is a continuation of the project thesis work that began in the fall semester of 2021. As a result, portions of the project thesis are reused in this study. The project thesis concentrated on preliminary work and developing a solid theoretical foundation. Hence, the introduction and theory are based on those used in the project thesis, although they have been refined and enlarged.

1.4 Structure of Thesis

The structure of the master thesis is as follows:

Chapter 2 presents the background theory for for Vortex Induced Vibrations and Computational Fluid Dynamics i.e. the numerical method.

Chapter 3 describes the validation cases conducted to ensure the numerical code works when working with a cylinder.

Chapter 4 gives a description of the preprocessing of the simulations regarding the computational domain, mesh, boundary conditions and numerical models.

Chapter 5 gives a short description of the tools used to post-process the results from simulations.

Chapter 6 contains the results from the simulations, sources of error and a brief discussion of the results.

Chapter 7 includes a conclusion of the thesis.

Chapter 8 contains suggestion to further work on the problem at hand.

2 Theory

In order to do a numerical investigation on VIV one must first learn the basics and that is why in this chapter both the fundamentals of VIV and theory of computational fluid dynamics (CFD) are presented.

2.1 Fundamentals of Vortex Induced Vibrations (VIV)

As risers with staggered buoyancy modules are indeed cylinders, it is important to know the basic theory behind flow around cylinders and this chapter covers this to some extent. The following chapter is mostly based on the book Hydrodynamics around cylindrical structures by Sumer and Fredsøe [20] with some input from [30], [32], [49], [12], [48].

2.1.1 Flow Around Circular Cylinders

The simplified scenario of a fixed circular cylinder exposed to a uniform steady flow is explored to understand the vortex shedding phenomenon better, as shown in Figure 1.
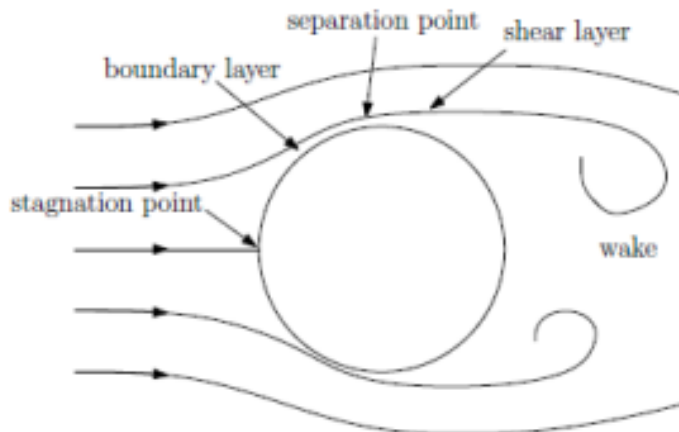
Figure 1: Steady flow around a fixed circular cylinder. Reprinted from Sumer and Fredsøe [20]

Potential flow theory states that the boundary conditions of impermeability and free-slip are valid on the body surface, which means that the flow velocity normal to the surface of the cylinder is equal to zero but that a tangential velocity exists [30]. The no-slip boundary condition states that the fluid velocity must be similar to the cylinder's speed and therefore go to zero, indicating that the potential flow theory is invalid in a practical instance where a fixed cylinder is considered. In other words, near the body, the fluid velocity must be lowered from its far-field value to zero within a predetermined distance, $\delta(x)$. A boundary layer (BL) is the term for the fluid layer of the thickness $\delta(x)$, and non-negligible viscous effects are seen there.

The shear/tangential stresses, which are proportional to the velocity gradient in the direction corresponding to the body surface, led to this observation.

Because of the enormous velocity gradients when the flow velocity decreases from the far field value to zero, shear stresses take significant discounts within the boundary layer. The thinner the boundary layer, the greater the shear stresses. The flow separation, which is the detachment of the boundary layer in a wake, is linked to creating the boundary layer as another significant phenomenon. Figure 1 is taken into account once more to provide more detail. The fluid flows in an adverse pressure gradient as it advances away from the stagnation point. When the boundary layer has traveled far enough along a negative pressure gradient that its speed in relation to the surface has stopped and reversed, the boundary layer separates. That is the point of flow separation. Following the flow's separation from the surface and the formation of a shear layer, eddies and vortices appear. The phenomena mentioned above, which result in the development of vortices, occur on both the top and lower sides of the body but with opposing vorticity directions.

From all that has been said so far [20], it is clear that the relative magnitude of the inertial and result forces is a crucial factor in the flow separation phenomena and, by extension, the shedding of vortices. The Reynolds number, determined by Equation 1 provides the ratio of those two forces, is an essential non-dimensional parameter.

$$Re = \frac{U \cdot D}{\nu} \qquad (1)$$

Where is the speed of the incoming flow, D is the characteristic length of the body and ν is the kinematic viscosity of the fluid. It is conventional practice to split the flow regimes by the size of the Reynolds number. According to Greco [30], the distinct flow regimes are provided as follows for flow past smooth circular cylinders.

- Sub-critical flow regime: $Re \lessapprox 2 \cdot 10^5$

- Critical flow regime: $2 \cdot 10^5 \lessapprox Re \lessapprox 5 \cdot 10^5$

- Super-critical flow regime: $5 \cdot 10^5 \lessapprox Re \lessapprox 3 \cdot 10^6$

- Transcritical flow regime: $3 \cdot 10^6 \lessapprox Re$

This is an acknowledged approach to classifying the regimes as it differs from literature to literature, but this is the most acknowledged approach. To better understand what happens in the different regimes, Figure 2 is presented.
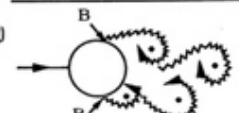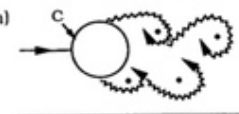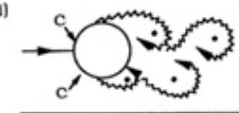
a)	No separation. Creeping flow	Re < 5
b)	A fixed pair of symmetric vortices	5 < Re < 40
c)	Laminar vortex street	40 < Re < 200
d)	Transition to turbulence in the wake	200 < Re < 300
e)	Wake completely turbulent. A:Laminar boundary layer separation	$300 < Re < 3\times10^5$ Subcritical
f)	A:Laminar boundary layer separation B:Turbulent boundary layer separation;but boundary layer laminar	$3\times10^5 < Re < 3.5\times10^5$ Critical (Lower transition)
g)	B: Turbulent boundary layer separation;the boundary layer partly laminar partly turbulent	$3.5\times10^5 < Re < 1.5\times10^6$ Supercritical
h)	C: Boundary layer completely turbulent at one side	$1.5\times10^6 < Re < 4\times10^6$ Upper transition
i)	C: Boundary layer completely turbulent at two sides	$4\times10^6 < Re$ Transcritical

Figure 2: Regimes of flow around a smooth circular cylinder in steady current. Reprinted from Sumer and Fredsøe [20]

For Reynolds numbers less than 5, no separation occurs [20]. The separation appears firstly when Re becomes five, and in the range of $5 < Re < 40$, we get a fixed pair of symmetric vortices with length increasing with the Reynolds number. For $40 < Re < 200$, periodic two-dimensional vortex shedding occurs, which means that it does not vary in the spanwise direction. As we move to higher Reynolds numbers the wake flow goes from laminar to turbulent, more precisely, when it exceeds 200. The boundary layer over the surface of the cylinder stays laminar from $300 < Re < 2\cdot10^5$, which is the subcritical flow regime. In this regime, the wake flow is wholly turbulent, and most experiments related to VIV take place in this regime [32] as Re further increases, the flow transitions to turbulent in the boundary layer as well. It starts at the separation point of the boundary layer. With increasing Re, it moves upstream towards the stagnation point as the Reynolds number increases

to $3 \cdot 10^5 < Re < 3.5 \cdot 10^5$ we get a turbulent boundary layer at the separation point, but only for one of the sides of the cylinder. The separation point changes from side to side, making the lift force change direction according to Schewe [39]. When the Reynolds number goes beyond $4.5 \cdot 10^6$, the boundary layer is thoroughly turbulent, and we have entered the transcritical regime.

2.1.2 Fundamentals of Vortex Shedding

In the above section, it has been written about the flow around a cylinder and the dominating phenomenon is vortex shedding. From Sumer and Fredsøe [20] the conclusion of separation of the boundary layer over a cylinder happens because of the adverse pressure gradient from the divergent flow environment at the rear end of the cylinder. A shear layer is created as a result. Significant amounts of vorticity are produced by the velocity dispersion in the boundary layer along the cylinder surface. This causes the shear layer to roll up into a vortex with the same sign as the incoming vortex when this vorticity convects into the shear layer created downstream of the separation point.
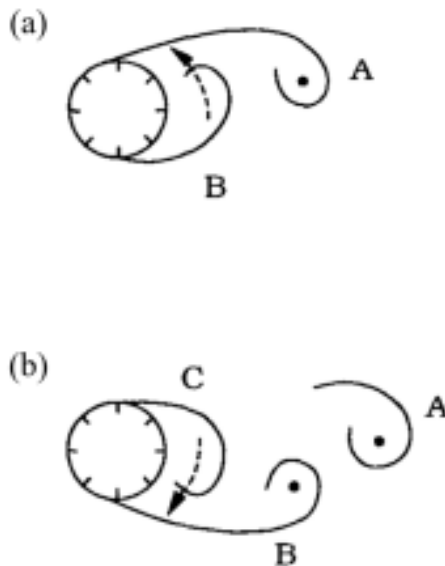
Figure 3: (a) Before shedding of Vortex A, Vortex B is being drawn across the wake. (b) Before shedding of Vortex B, Vortex C is being drawn across the wake (Reproduced from Sumer and Fredsøe [20]

Gerrard [21] was the first one to describe the process of vortex shedding behind a circle. The velocity dispersion in the boundary layer along the cylinder surface produces significant amounts of vorticity side and consequently drag the other vortex across the wake as illustrated in Figure 3(a). Here Vortex A, which rotates in the clockwise direction, grows larger than Vortex B, which rotates in the counterclockwise direction and drags Vortex B across the wake. As Vortex B is dragged closer to vortex A it cuts off the vorticity of vortex A and causes Vortex A to shed. As Vortex A sheds, a new Vortex C will form on the same side as Vortex A as indicated

in Figure 3(b). This will make the same shedding happen to Vortex B as Vortex A and this will continue to alternate between the two sides of the cylinder at a certain frequency causing a force than will be mentioned later.

2.1.3 Vortex Shedding Frequency

The vortex shedding frequency can be seen as a function of the Reynolds number [20]:

$$St = St(Re) \tag{2}$$

where

$$St = \frac{f_v D}{U} \tag{3}$$

and U is the flow velocity, D is the cylinder diameter and ,f_v is the vortex-shedding frequency. The Strouhal number (St) is the normalized vortex-shedding frequency. In Figure 4, it is illustrated how the Strouhal number varies with the Reynolds number.
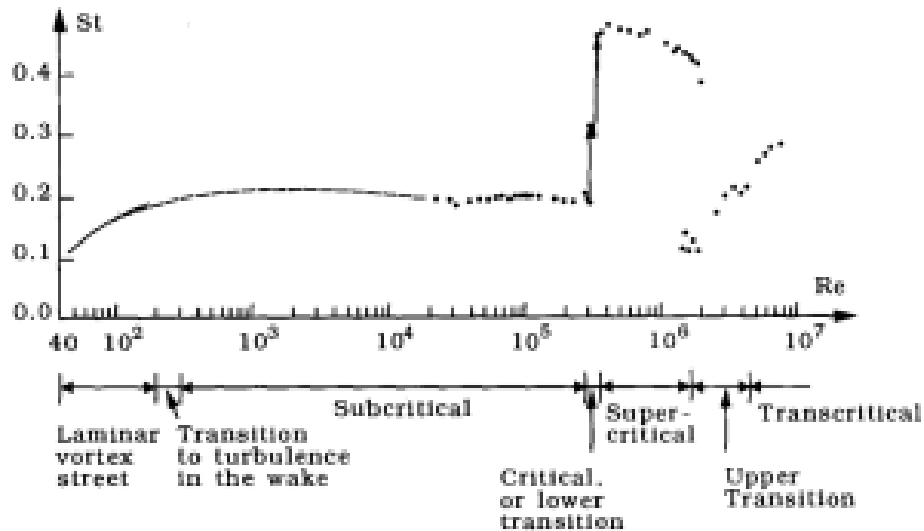
Figure 4: Strouhal number for a smooth circular cylinder. Solid curve from Williamson, the dashed curve from Roshko, and the dotted curve from Schewe. Reproduced from Sumer and Fredsøe [20]

From Figure 4, we can see how the Strouhal number is approximately 0.1 at $Re = 40$, and then it increases up to about 0.2 for a Reynolds number of 10^3. From there, it is somewhat constant until around $Re = 3 \cdot 10^5$ when it more than doubles. This is in the critical Re range found in Figure 2, and afterward it decreases gradually with higher Reynolds numbers.

2.2 Forces From Vortex Shedding

A body in a steady, uniform flow would typically experience drag and lift forces that are parallel and perpendicular to the direction of the incoming flow [20]. Independent of time, their mean values per unit length are stated as follows:

$$\bar{F}_D = \frac{\rho}{2} C_D D U^2 \tag{4}$$

$$\bar{F}_L = \frac{\rho}{2} C_L D U^2 \tag{5}$$

where the fluid density is ρ, D is the he cross sectional length,h which is equal to the diameter of a circular cylinder, U is the incoming velocity, and the empirically determined drag and lift coefficients, are C_D and C_L.

The body that the incoming fluid flows around will feel oscillatory forces because of the periodic variations in pressure on the body when the vortex shedding has an apparent periodicity, i.e., there is only one vortex shedding frequency. Therefore, in addition to a mean component, the drag and lift force will also contain an oscillating part with specific amplitudes A_D and A_L as stated in the previous section. The lift force will oscillate with a frequency that is equal to the vortex shedding frequency, f_s, while the drag force will oscillate with a frequency that is twice as high according to Greco [30]. The direction of the lift force caused by a vortex will depend on which side of the body the vortex is shed, which is why the drag force and lift force oscillate at different frequencies. The drag force is independent of the side on which vortex shedding occurs. Since the lift and drag forces consist of a static and dynamic term, they can thus be effectively approximated by the equations provided in Equations 6 and 7

$$F_D = \bar{F}_D + A_D cos(4\pi f_s t + \beta_D) \tag{6}$$

$$F_L = \bar{F}_L + A_L cos(2\pi f_s t + \beta_L) \tag{7}$$

2.2.1 The Result of Vortex Shedding: VIV and VIM

Vortex-induced lift and drag forces are applied to a fixed body when exposed to an incident flow, as previously discussed. The forces mentioned above will cause structural oscillations in both the cross-flow and in-line directions, assuming the body is not restrained. These motions are classified as resonant phenomena if the body oscillates at its natural frequency. The vortex-induced motions (VIM) and the vortex-induced vibrations (VIV) are typically used to categorize these vortex-induced resonances. The distinction between these two phenomena, according to DNV's VIV Best Practice [32], is in the oscillation frequency. Any large-diameter body exposed to current can experience VIM. This is usually for semisubs and spar

buoys. On the opposite side, VIV is characterized by a substantially larger oscillation frequency and mostly involves elastic motions of slender structures, such as pipes, risers, and mooring lines. There are two types of VIV, cross-flow and in-line. They are both presented in Figure 6.
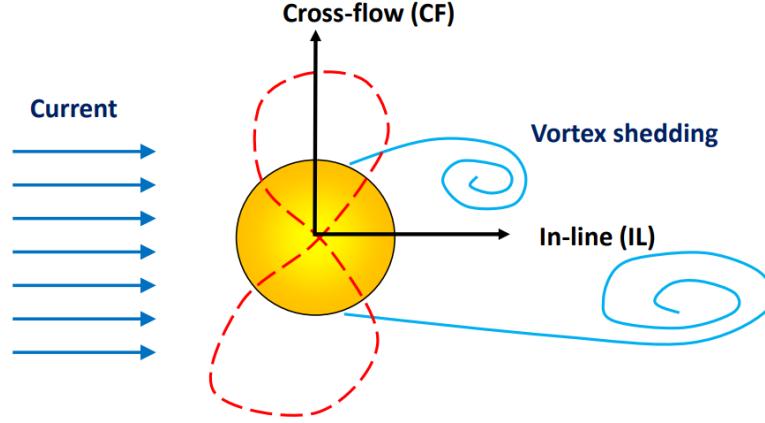
Figure 5: Presentation of Cross-flow and In-line vibrations. Reprinted from Sintef Powerpoint on Vortex induced vibrations [40]

When the oscillation frequency f_s of the lift force equals the structure's natural frequency $f_{n,y}$ in the direction opposite the incoming flow, cross-flow (CF) VIV develops. Accordingly, in-line (IL) VIV happens when the drag force oscillation frequency $2f_s$ equals the structure's in-line natural frequency $f_{n,x}$. It should be emphasized that since VIV causes lock-in, these criteria are solely intended to show which frequency ranges VIV occurs for. The phenomenon known as lock-in occurs when a vortex's shedding frequency latches onto the structure's inherent frequency. This have a strong connection to the reduced velocity U_R which is stated as

$$U_R = \frac{U}{f_n D} \qquad (8)$$

where U is the velocity of the flow, D is the diameter of the cylinder and f_n is the natural frequency of the cylinder. Considering that, for a fixed cylinder, the vortex shedding frequency grows linearly with the flow velocity, as shown in Equation 8, lock-in can be stated in simple terms. However, the interaction between the cylinder's structural oscillations and the vortex shedding process causes the variables to depart from the linear connection and synchronize or lock with the cylinder motion, where their frequencies eventually become equal.
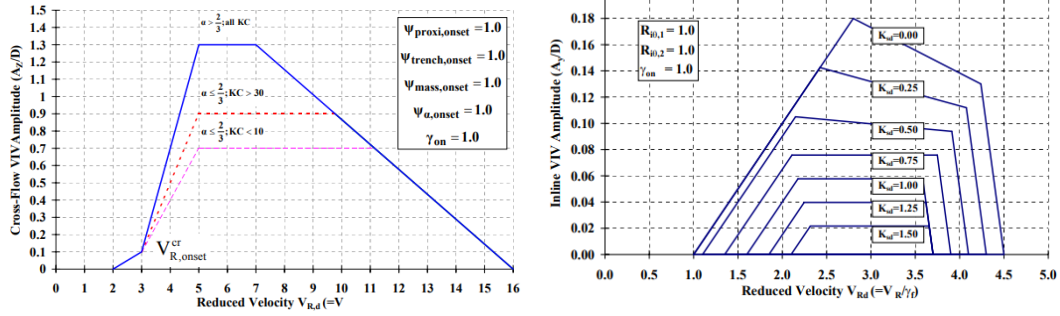
Figure 6: CF and IL VIV Response amplitudes as a function of reduced velocity. Reprinted from DNV's Recommended Practice: Free spanning pipelines [14]

Figure 6 presents the CF and IL VIV as a function of reduced velocity on a circular cylinder. Crossflow VIV occurs in a reduced velocity range of 2 –16 with a higher response amplitude than IL VIV. Research has found that VIV changes the natural period of the body in water [49]. This is because the added mass changes with the vibrations; thus, the natural frequency changes. This is represented in Figure 7 found by Ming [49] where CF vibrations are investigated for a selected range of reduced velocity and a constant Reynolds number of 500.
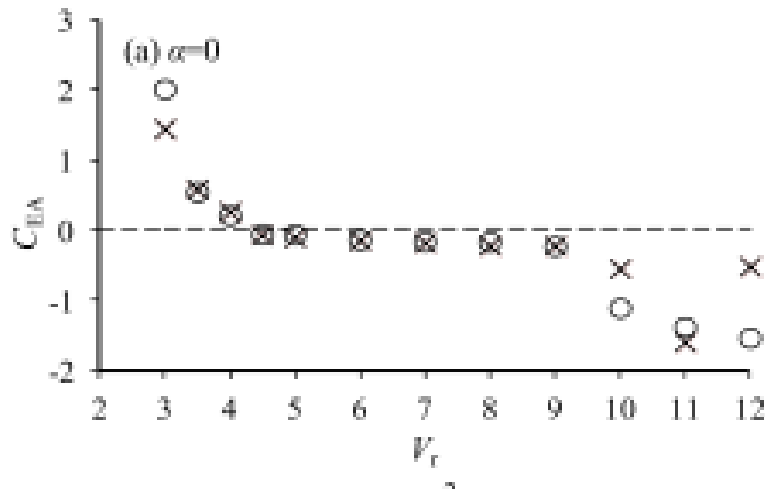
Figure 7: Added mass coefficient as a function of reduced velocity. Reprinted from Ming [49]

2.2.2 Added Mass and Excitation Coefficients

The effective increase in the apparent mass of a solid entity when immersed or surrounded by a fluid or gas is referred to as added mass. When a solid item moves through a fluid medium, such as water or air, it displaces the surrounding medium and encounters resistance from the displaced fluid's inertia. This extra resistance is referred to as added mass [48].

The added mass is an apparent increase in the mass of the object that impacts

its dynamic behavior. It results from the object's coupling with the surrounding fluid, and it is especially relevant when the object's motion generates large-scale fluid displacements. The magnitude of the extra mass is determined by a number of factors, including the shape and size of the item, the density and viscosity of the fluid, and the relative velocity of the object and the fluid.

The definition of the added mass coefficient C_a from the oscillating pipe with a harmonic motion at one oscillation period from t_n to t_{n+1} can be written as

$$C_a = \frac{\frac{2}{T} \int_{t_n}^{t_{n+1}} F_y(t)\ddot{y}(t)dt}{\rho \frac{\pi}{4} D^2 L (y_0 \omega^2)^2} \tag{9}$$

where T is the oscillation period, F_y is the force, $\ddot{y}$ is the oscillating acceleration, y_0 is the amplitude of harmonic oscillation and ω is the angular frequency of the harmonic oscillation.

The excitation coefficient is an expression used frequently in the study of vibrations and the dynamic response of structures immersed in fluid. It is connected to the additional mass notion and represents the fluid's efficiency in exciting the structure [48].

When a structure interacts with a fluid flow, dynamic forces and moments occur that can cause vibrations. Variables such as fluid flow turbulence, vortex shedding, and fluid-structure interactions can all create these vibrations. The excitation coefficient quantifies the link between the fluid's dynamic forces and the consequent structural response.

The definition of the excitation coefficient from the oscillating pipe at one oscillation period from t_n to t_{n+1} can be written as

$$C_{Lv} = \frac{\frac{2}{T} \int_{t_n}^{t_{n+1}} F_y(t)\dot{y}(t)dt}{(\frac{1}{2}\rho D L U^2) y_0 \omega} \tag{10}$$

where $\dot{y}$ is the oscillating velocity.

2.3 Computational Fluid Dynamics (CFD)

The technique of numerically solving the equations of interest, in this case, the Navier-Stokes equations, is known as computational fluid dynamics (CFD). CFD knowledge has been around for a while, but it wasn't until the adoption of high-speed computers that solving fluid dynamical issues became a reality. The capacity to tackle intricate physics and obtain the time evolution of the flow is the advantage of numerically solving fluid dynamic problems over analytical and experimental methods. However, its drawbacks include truncation errors, boundary condition difficulties, and high computing costs for complex geometries [3].

This section presents a general theory about the program STAR-CCM+, Navier-Stokes equations, turbulence models, and some methods used in CFD.

2.3.1   Star-CCM+

CD-adapco created the commercial CFD software STAR CCM+ to run extensive simulations efficiently. The software uses object-oriented programming, making it accessible to amateurs and specialists. CAD modeling, CAD embedding, surface preparation tools, automatic meshing models, physics modeling, turbulence modeling, and post-processing of the simulation results are all covered by the software.

Solving the Navier-Stokes equations is made possible by a variety of choices offered by Star-CCM+. These include inviscid potential flow, large eddy simulation (LES), detached eddy simulation (DES), and multiple Reynolds Averaging models (RANS) [1].

2.3.2   Governing Equations

The governing equations for viscous fluid flow are the Navier-Stokes (N-S) equations and the Continuity Equation [30]. The N-S equations describe the fluid's motion in terms of the conservation of momentum, whereas the continuity equation represents the conservation of mass. A few presumptions relating to the fluid characteristics can be made for simplicity, and in relation to this thesis, simplifications about the fluid characteristics can be made. The fluid of interest in this instance is seawater. It is acceptable to suppose that the density is constant over the entire domain, that is, incompressible. Additionally, the kinematic viscosity v and the dynamic viscosity η are considered a constant across the entire domain, i.e. Newtonian. In addition to these presumptions, the fluid is assumed to be isothermal, which allows for the disregard of fluctuations in fluid temperature. Therefore, no extra differential equations are required to describe energy conservation. Then the Navier-Stokes equations can be written as:

$$x-direction: \frac{\partial u}{\partial t} + u\frac{\partial u}{\partial x} + v\frac{\partial u}{\partial y} + w\frac{\partial u}{\partial z} = -\frac{1}{\rho}\frac{\partial p}{\partial x} + g_x + \nu(\frac{\partial^2 p}{\partial x^2} + \frac{\partial^2 p}{\partial y^2} + \frac{\partial^2 p}{\partial z^2}) \quad (11)$$

$$y-direction: \frac{\partial v}{\partial t} + u\frac{\partial v}{\partial x} + v\frac{\partial v}{\partial y} + w\frac{\partial v}{\partial z} = -\frac{1}{\rho}\frac{\partial p}{\partial y} + g_y + \nu(\frac{\partial^2 v}{\partial x^2} + \frac{\partial^2 v}{\partial y^2} + \frac{\partial^2 v}{\partial z^2}) \quad (12)$$

$$z-direction: \frac{\partial w}{\partial t} + u\frac{\partial w}{\partial x} + v\frac{\partial w}{\partial y} + w\frac{\partial w}{\partial z} = -\frac{1}{\rho}\frac{\partial p}{\partial z} + g_z + \nu(\frac{\partial^2 w}{\partial x^2} + \frac{\partial^2 w}{\partial y^2} + \frac{\partial^2 w}{\partial z^2}) \quad (13)$$

and the Continuity Equation can be written as:

$$\frac{\partial u}{\partial x} + \frac{\partial v}{\partial y} + \frac{\partial w}{\partial z} = 0 \tag{14}$$

Newton's second law of motion, which describes the relationship between a body with applied forces and the motions in reaction to those forces, is the basis of the N-S equations. The unstable term is the first term in the equation. The following three terms on the left side are terms for acceleration. The pressure term, the body force term, and the viscous term are the three terms on the right side. The body force (gravity) term is frequently ignored.

2.3.3 Reynolds Averaged Navier Stokes (RANS)

Reynolds-Averaging is built on the time-averaged equations of motion for fluid flows. The method's goal is to break down the N-S equations into a time averaged and a fluctuating quantity [12]. This mathematical operation can be completed by assuming that a parameter's instantaneous value can be expressed as the sum of its mean and fluctuating values. As a result, the N-S equations can be recast as

$$\frac{\partial \tilde{u}_i}{\partial t} + \tilde{u}_j \frac{\partial \tilde{u}_i}{\partial x_j} = -\frac{1}{\rho} \frac{\partial \tilde{p}}{\partial x_i} + \nu \frac{\partial^2 \tilde{u}_i}{\partial x_j \partial x_j} \tag{15}$$

where the instantaneous velocity is $\tilde{u}_i$. The sum of this value has a mean and fluctuating part shown as

$$\tilde{u}_i = U_i + u_i \tag{16}$$

Performing the same principle of time averaging for all terms in the Navier-Stokes equations by applying the rules of Reynolds averaging, the equation can be simplified. Furthermore, the equation can be simplified by the simplification that the fluctuations and the mean velocity conserve mass i.e. $\partial U_i / \partial x_i = 0$ and $\partial u_i / \partial x_i = 0$. These simplifications give the Reynolds Averaged Navier-Stokes equation as

$$\frac{\partial U_i}{\partial t} + U_j \frac{\partial U_i}{\partial x_j} = -\frac{1}{\rho} \frac{\partial}{\partial x_j} (-P\delta_{ij} + \mu(\frac{\partial U_i}{\partial x_j} + \frac{\partial U_j}{\partial x_i}) - \rho \bar{u_i u_j}) \tag{17}$$

where the first term on the right side is the pressure stress, the second term is the viscous stress and the third is the turbulent stress. The most significant term is the turbulent stress as it models the turbulence of the fluid. As turbulence is non-linear with no analytical solution it is this part of turbulence modeling that is the most difficult.

2.3.4 Turbulence Modeling

Without using turbulence models, it is almost impossible to solve turbulent flows in practical engineering [11]. Various turbulence models are available to model various flow behaviors, depending on the processing power and needed simulation accuracy. The different models will need varying amounts of computational power, ranging from fully numerically solved Navier-Stokes equations to a high level of simulating the influence of the turbulence. While Direct Numerical Simulation (DNS) directly solves the equations for turbulent flow, Reynolds-Averaged Navier Stokes (RANS) models, Large Eddy Simulation (LES) and Detached Eddy Simulation (DES) models the influence of the turbulence [5]. Due to its great computational costs, DNS is mostly used in high-end research.

The major turbulence models of the RANS-solver approach in Star-CCM+ to the Navier-Stokes equations are the $k - \epsilon$, $k - \omega$, Reynolds Stress Transport, and Spalart-Allmaras turbulence models [1]. Every model has a unique set of strengths and weaknesses and is employed in a variety of simulations. Depending on the flow mechanics and the boundary layer profile, some tlence models are designed for a particular level of y+-values, giving an upper range of applicability for the y+-value.

The realizable $k - \epsilon$ model and $k - \omega$ SST are the two primary turbulence models employed in the RANS solution. The $k - \epsilon$ model was by far the most often used technique to simulate the mean flow characteristics for turbulent flow conditions until the last decade of the twentieth-century [46]. The transport equations for the turbulent kinetic energy k and the turbulent dissipation rate ϵ are solved by this two-equation model [1]. The $k - \epsilon$ turbulence model comes in many different variations that are tailored for various factors including Reynolds number and y+ value. With an all-y+ wall treatment, realizable two-layer $k - \epsilon$ is frequently employed for increased versatility.

Another widely employed two-equation turbulence model is $k - \omega$. The fact that this model can be used in the viscous-dominated region of the boundary layer without any adjustments is a considerable advantage. This model has been observed to perform better for boundary layers under adverse pressure gradients than the $k - \epsilon$ model, which is an added benefit [1].

The $k - \omega$ SST model was created as an advancement over the two models discussed above. The $k - \omega$ SST model improves the model and offers improved separation prediction by addressing the advantages and disadvantages of $k - \omega$ and $k - \epsilon$. In this turbulence model, a $k - \epsilon$ model in the far field is combined with a $k - \omega$ model next to the wall [1]. This model makes sure that both the near-wall and far-field zones are adequately resolved by including an additional cross-diffusion term in the equation [7].

2.3.5 Large Eddy Simulation (LES)

The chosen turbulence model used in this thesis is the Large Eddy Simulation with a Smagorinsky subgrid scale model and the theory behind it will be presented below.

Conservation of mass for an incompressible and isothermal flow can, according to Ferziger et al [17] be written as

$$div\,\vec{v} = 0 \tag{18}$$

and momentum conservation is given as

$$\frac{\partial u_i}{\partial t} + div\,(u_i\vec{v}) = div\,(\mu\,grad\,u_i) - \frac{1}{\rho}\,div\,(p\vec{i_i}) + b_i \tag{19}$$

Turbulent flows have a wide variety of length and time ranges. The left side of Figure 8 shows a schematic representation of the length scales of eddies that may be encountered in the flow. The velocity component at a fixed point in the flow is shown on the right side of the figure to demonstrate the time dependence.
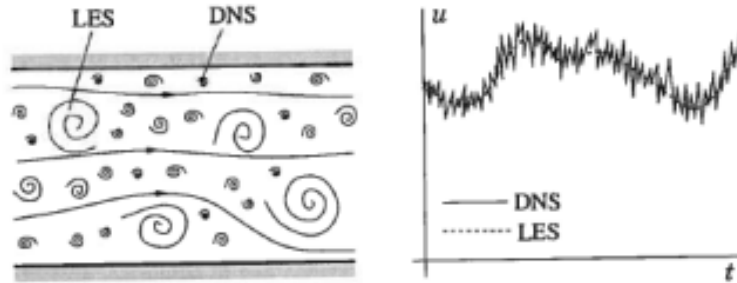
Figure 8: Turbulent motion and time dependancy. Reprinted from Ferziger et al [17]

The large-scale motions in turbulence are far more powerful than the small scales. Large-scale eddies are stronger than small ones, making them better carriers of preserved properties. Therefore, it makes sense to simulate large eddies differently from small ones, and the Large Eddy Simulation (LES) method does just that. Even tho LES is expensive it is a lot less expensive than direct numerical simulation (DNS). LES is time-dependent and three-dimensional, when working with complex geometry or too high Reynolds numbers for DNS, it is preferred to use LES.

The velocity field must only include the large scale features of the overall field in order to use LES. Filtering is used for this. A local average of the entire field will be used to simulate the big scale field. Ferziger et al [17] provide a description of the filtering principles.

The filter is linked to a length scale Δ. Eddies bigger than Δ are considered large eddies, while those smaller than Δ are considered small eddies. The smaller ones will have to be modelled. The constant density filtered Navier-Stokes equations are highly comparable to the Reynolds-Averaged Navier-Stokes equations as they are written as

$$\frac{\partial(\rho\overline{u_i})}{\partial t} + \frac{\partial(\rho\overline{u_i u_j})}{\partial x_j} = -\frac{\partial\overline{p}}{\partial x_i} + \frac{\partial}{\partial x_j}[\mu(\frac{\partial\overline{u_i}}{\partial x_j} + \frac{\partial\overline{u_j}}{\partial x_i})] \tag{20}$$

The continuity equation is linear and does not change substantially

$$\frac{\partial(\rho\overline{u_i})}{\partial x_i} = 0 \tag{21}$$

In the filtered Navier-Stokes equation $\overline{u_i u_j} \neq \overline{u_i}\,\overline{u_j}$. It is modeled an approximation for the dissimilarity of the two sides of the inequality written as

$$\tau_{ij}^s = -\rho(\overline{u_i u_j} - \overline{u_i}\,\overline{u_j}) \tag{22}$$

where τ_{ij}^s is the subgrid scale Reynolds stress (SGS stress). The term "stress" refers to how it is addressed rather than its physical nature. It is, in fact, the large-scale momentum flow induced by the activity of small or unresolved scales. The term "subgrid" can be perplexing. Other than the fact that $\Delta > h$, the width of the filter has nothing to do with the grid size h. Subgrid scale (SGS) models are the models that are used for estimating the SGS stress [17]

2.3.6   The Smagorinsky Subgrid Scale Model

The Smagorinsky subgrid scale model is the most often used SGS model. This is an eddy viscosity model, which assumes that the impacts of the SGS Reynolds stress are increased dissipation and transport. Because increased transport and dissipation are impacts of viscosity in laminar flows, Ferziger et al [17] propose the following model

$$\tau_{ij}^s - \frac{1}{3}\tau_{kk}^s\delta_{ij} = \mu_t(\frac{\partial\overline{u_i}}{\partial x_j} + \frac{\partial\overline{u_j}}{\partial x_i}) = 2\mu_t\overline{S_i} \tag{23}$$

where μ_t is the eddy viscosity.

The subgrid scale viscosity is then given by

$$\mu_t = C_S^2\rho\Delta^2\left|\bar{S}\right| \tag{24}$$

where C_S is the model parameter, Δ is the filter length scale and $\left|\bar{S}\right| = (\bar{S}_{ij}\bar{S}_{ij})^{1/2}$. In this thesis' simulations, C_S is set to 0.1 because of recommendations from CD-adapco [1].

2.3.7 Detached Eddy Simulation (DES)

Standard LES models could struggle in locations that are near to a wall. The grid in the boundary layer must have a high resolution, typically y+ 1, because LES does not use wall functions [33]. Additionally, an LES simulation must be run for a long enough flow period to produce consistent flow data. As a result, executing LES simulations requires more computing power than steady RANS simulations.

Hybrid models that combine the unsteady RANS models in the boundary layer and LES treatment in the separated regions have been developed in order to achieve both the benefit of a coarser mesh in the outer region (achieved by LES) and to avoid the need for a high grid resolution in the boundary layer (RANS models). Such a hybrid model is Detached Eddy Simulation (DES), developed by Spalart et al [33].

2.3.8 Mesh Morphing

A mesh is a collection of interconnected vertices, edges, and faces that represents a three-dimensional object or surface. Mesh morphing is a method used in computer animation and engineering models to change the shape or structure of a mesh. Mesh morphing is frequently used to seamlessly transition or interpolate between several mesh topologies, enabling more precise and realistic representations of intricate systems and procedures [37].
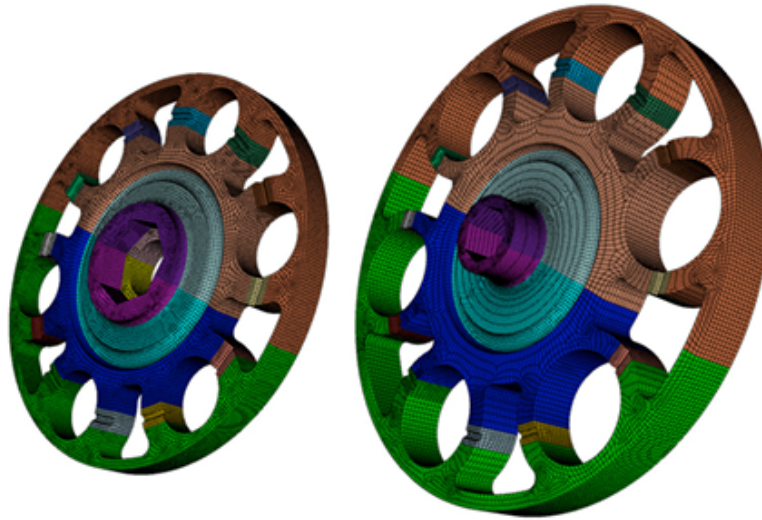
Figure 9: Simple capture of mesh morphing, the mesh to the left changes according to the change in geometry to the right. Reprinted from Staten et al [41]

There are various techniques for doing mesh morphing, each with its own set of benefits and drawbacks. Some of the most common methods are linear interpolation, which moves the mesh's vertices along straight lines between the initial and final shapes; non-linear interpolation, which moves the vertices along curved paths that

better capture the overall shape changes; and mesh warping, which distorts the mesh's edges and faces to better match the intended shape.

Mesh morphing is a valuable tool for modeling the deformation and movement of objects in general, such as when analyzing fluid flow around a moving object or designing flexible structures. It can also be used in other fields such as animation, video game creation, and medical imaging.

2.3.9   Arbitrary Langrangian-Eulerian method (ALE)

The Lagrangian formulation and the Eulerian formulation are two distinct ways to represent continuum materials mathematically. The Lagrangian technique makes it simple to follow individual material particles because the coordinate system moves with the materials. Instead, with the Eulerian approach, the coordinate system is fixed, and the material particles move across a stationary, closed domain. A purely Lagrangian method for the kinematic description of the fluid domain is not capable of efficiently tracking powerful distortions occurring frequently in the fluid domain [16]. This is because the main drawback of the Lagrangian description is that it suffers from following large distortions in the computational domain. Furthermore, because the coordinate system is stable in space and convection terms are employed to explain the fluid transport, when fluid motions are represented in Eulerian coordinates, significant distortions can be handled with ease [16]. The governing equations for fluid flow can be modeled using a completely Eulerian formulation when an ALE formulation is applied to fluid structure interaction, while the structure domain is treated using a purely Lagrangian formulation. A combination of the Lagrangian and Eulerian methods is provided by the arbitrary Lagrangian-Eulerian (ALE) approach [25]. The ALE technique's coordinate system is linked to a moving mesh, enabling a seamless transition from the Lagrangian method to the Eulerian method.

To provide a fluid grid that conforms to the body, the ALE approach allows the fluid grid to deform at any velocity. The important benefit of a body-conforming grid is the correlation of the moving boundary with the grid lines, allowing the computation to appropriately account for geometric discontinuities. Additionally, the study of variables at the moving boundary, such as wall shear stress and pressure, does not require approximation.

2.3.10   Immersed Boundary Method

Even when employing a Cartesian grid, the immersed boundary approach (IBM) allows the effect of the body on the flow to be taken into consideration [35]. This method of solving the boundary conditions on the body stands out because it allows the solver to run the entire simulation on a constant Cartesian grid, which significantly reduces the amount of computation required. By directly applying the immersed boundary method, the boundary conditions from the body to the Cartesian fluid cells are interpolated. An unstructured triangular mesh is used to represent the geometry's surface, and cells of a Cartesian grid are used to represent

the fluid domain. The immersed boundary method applies the geometry directly to
the block cells [9].

2.3.11 The Supercomputer Betzy

A substantial amount of computer resources were required to apply LES to the three-
dimensional investigations in this thesis. As a result, the analyses were carried out
on the supercomputer Betzy. Jobs are sent to a queue in order to execute analyses.

Betzy, an Atos-provided supercomputer that is a BullSequana XH2000, offers Nor-
wegian researchers significantly increased computational capacity, boasting a theor-
etical peak performance of 6.2 PetaFlops. It is known as the most powerful super-
computer in Norway named after Mary Ann Elizabeth Stephansen, the first Nor-
wegian woman awarded a doctorate degree. Housed at NTNU in Trondheim, this
state-of-the-art supercomputer became operational on November 24, 2020. With its
enhanced capabilities, Betzy furnishes researchers with nearly triple the previous
computational power, facilitating close to two billion CPU hours annually. The su-
percomputer's operational tenure spans four years until 2024, with the potential for
a one-year extension until 2025.

The use of Betzy in this thesis has decreased the computational time running the
simulations a lot compared to using a workstation at NTNU Moholt. Below are
some of the stats for Betzy listed.

- System: BullSequana XH2000

- Max Floating point performance, double: 6.2 Petaflops

- Number of compute nodes: 1344

- CPU type: AMD Epyc 7742 2.25GHz

- CPU cores in total: 172032

- CPU cores per node: 128

- Memory in total: 336 TiB

- Memory per node: 256 GiB

- GPU type: Nvidia A100 40 GB with NVLink

- GPUs per node: 4

- GPUs in total: 16

- Operating system: Red Hat Enterprise Linux 7

- Total disc capasity: 2.5 PB

- Interconnect: InfiniBand HDR 100, Dragonfly+ topology

3 2D Validation Cases

Validation cases play a vital role in the field of CFD to ensure the accuracy and reliability of numerical simulation tools. In the context of fluid flow analysis, studying laminar flow at different Reynolds numbers is of great importance. The Reynolds number, a dimensionless quantity that relates the inertial and viscous forces in a fluid flow, provides valuable insights into the flow regime and behavior.

These validation cases aim to investigate laminar flow at two distinct Reynolds numbers: 40 and 50. The results from these simulations will be compared to previous research for the validation of the code to ensure the reliability of the code STAR-CCM+.

3.1 Physical Models

As this is a 2D laminar flow case the physical models applied are somewhat different from the 3D turbulent case. The selected models are listed below.

- Equation of state: Constant density

- Time: Implicit unsteady

- Viscous regime: Laminar

- Flow: Segregated flow

- Space: Two dimensional

3.2 Computational domain

The computational domain used in the validation cases is chosen after reviewing other publications on simulations of flows with low Reynolds numbers. Constant et al [13] provide a benchmark for the computational setup for the low Reynolds number cylinder situation. The computational domain has a rectangular form with [-20D, 40D] x [-20D, 20D] in the x and y dimensions. The domain's upstream, downstream, and lateral dimensions are carefully set to avoid any interference from boundaries. The chosen computational domain is illustrated in Figure 10
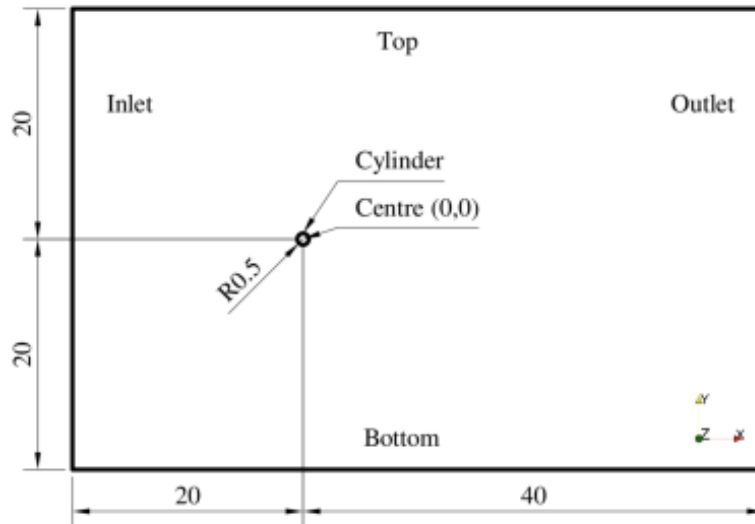
Figure 10: Computational domain of both the validation cases. Reprinted from Park et al [34]

3.3 Mesh

The mesh used in the validation cases is a polygonal mesh with a prism layer in the boundary layer of the cylinder as illustrated in Figure 11. The Polygonal Mesher in STAR-CCM+ captures complicated geometries properly while enabling mesh refining and adaptability flexibility. Engineers and scientists can use this feature to do simulations in a variety of fields, including automotive design, aerospace engineering, and environmental studies, where complicated or irregular geometries are encountered [1]. Prism layers, also known as boundary layer meshes, are often employed in computational fluid dynamics (CFD) simulations for meshing around circular or curved geometries. These layers of mesh components give various advantages that improve the simulation's accuracy and efficiency, such as capturing the boundary layer flow [1].

Figure 11: Close up of mesh around the cylinder.

3.4   Initial Conditions and Boundary Conditions

The two cases describe a circular cylinder in infinite fluid with uniform flow. The cases in question are two-dimensional, with Reynolds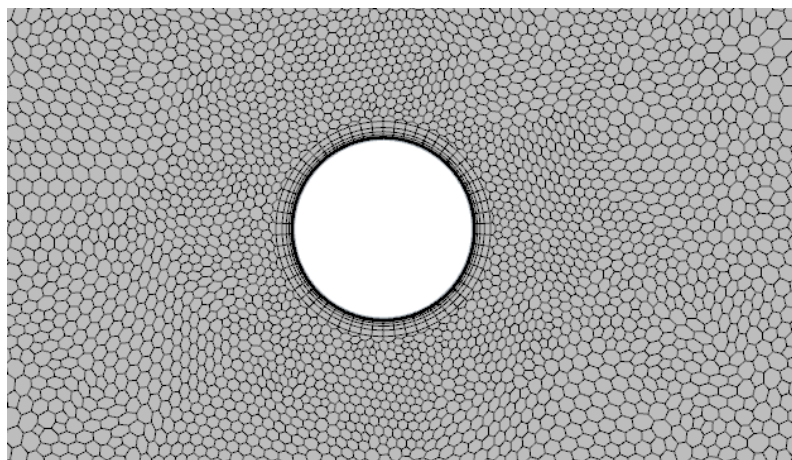 numbers of 40 and 50, indicating that the flow regime is laminar and the boundary layer over the cylinder is laminar. The diameter, D, is fixed at 0.1 m, the incoming flow has a fixed velocity of 1 m/s and the density is kept constant to 1000 kg/m^3 in the following study. The parameter μ were scaled to achieve Reynolds numbers 40 and 50. In Table 1 all parameters are displayed.

Table 1: Physical parameters for validation cases.

Physical parameters for validation cases					
Case	U [m/s]	D [m]	ρ [kg/m^3]	μ [kg/ms]	Re [-]
40 Re	1.0	0.1	1000	2.5	40
50 Re	1.0	0.1	1000	2.0	50

The selected boundary conditions used in the validation cases are listed below.

- Inlet: Velocity Inlet. Constant velocity: 1.0 m/s

- Outlet: Pressure outlet

- Top and bottom: Symmetry plane

- Front and back: Symmetry plane

- Cylinder: Wall

3.5   2D Validation Results

Below are two short chapters on the results from the validation cases and how they compare to previous research.

3.5.1   Case 1: 40 Reynolds

The numerical model for the case with a Reynolds number of 40 is firstly compared to how the flow behaves. This is compared with Sumer and Fredsøe's [20] description of vortices behind a cylinder at Reynolds number 5 to 40 from Chapter 1 in Figure 2.

In Figure 12 the streamlines from the case are illustrated and they are in good agreement with the theoretical behavior of the flow as two symmetrical vortices appear in the wake.
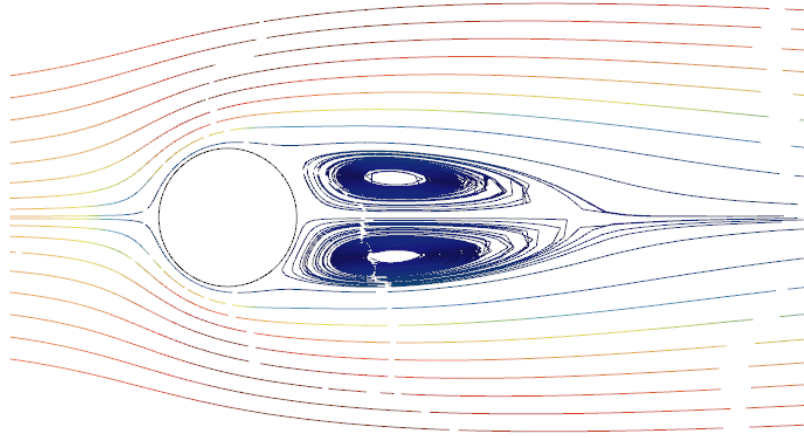
Figure 12: Stream lines forming in the wake of the cylinder.

Secondly, the results are compared to the drag coefficient on the cylinder with previous research. In Table 2 a series of drag coefficients from research by others are compared to the present one. This looks to be in good agreement with the former experiments as the drag coefficient is quite similar.

Table 2: Present study compared to earlier studies.

Study	C_D
Present	1,53
Tritton [43]	1,48
D & Chang [15]	1,52
Fornberg [18]	1,50
He & Doolen [24]	1,50
Ye et al [47]	1,52

Thirdly, the results from this simulation are compared with respect to the pressure distribution around on side of the cylinder from the stagnation point to the back of the cylinder in the x-direction. Grove et al [23] researched this experimentally and are therefore the research compared to.

In Figure 13 the pressure coefficient distribution is compared with Grove et al's [23] measurements and they compare well to the experimental results.
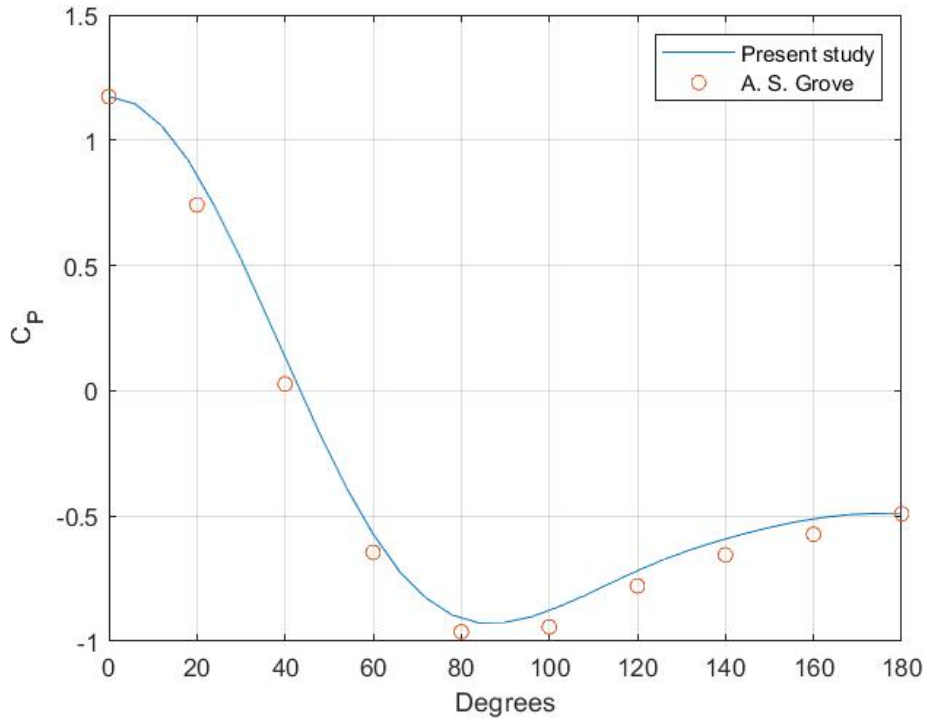
Figure 13: Comparison of the pressure distribution around the cylinder.

3.5.2   Case 2: 50 Reynolds

The numerical model for the case with a Reynolds number of 50 is also firstly compared to how the flow behaves. This is compared with Sumer and Fredsøe's [20] description of vortices behind a cylinder at Reynolds number 40 to 200 from Chapter 1 in Figure 2.

As illustrated by the streamlines around the cylinder in Figure 14 the vortex street is beginning to form but is still quite calm. As the Reynolds number is only 50 the big vortices are yet to be formed but there are some resemblances to the theory from Sumer and Fredsøe [20] where a laminar vortex street appear and vortices on each side of the cylinder separate periodically.

Figure 14: Scalar scene of streamlines showing the flow in the wake of the cylinder.

Secondly, the numerical results from this simulation are compared to the numerical findings of Qu et al [36]. They did numerous numerical simulations on flow past a circular cylinder from Reynolds numbers ranging from 50 to 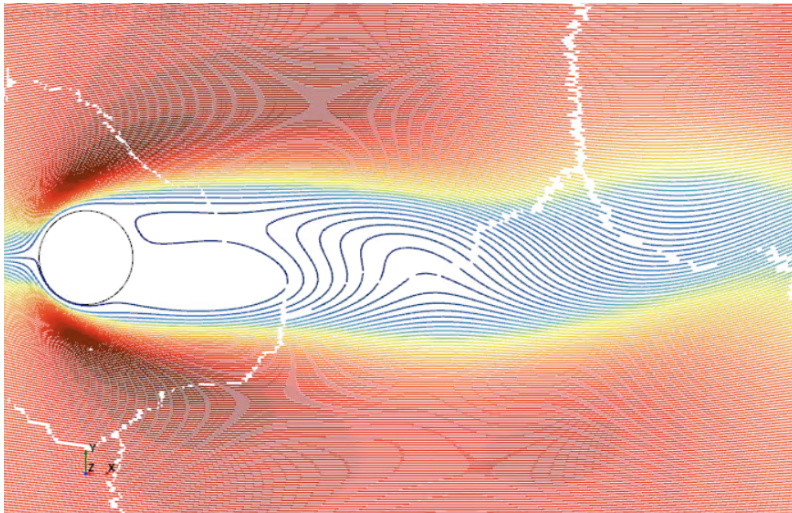200. The findings are compared to the present validation case concerning the drag coefficient C_D, lift coefficient C_L and the Strouhal number St. The result of the comparison are presented in Table 3 and they are in good agreement with each other as they do not differ a lot regarding lift and drag coefficient and Strouhal number.

Table 3: Present study compared to earlier studies.

Study	C_D	C_L	St-number
Present	1,420	0,043	0,123
L. Qu et al [36]	1,397	0,040	0,124

3.6 Conclusion of Validation Cases

In conclusion, this validation study focused on investigating the flow characteristics over a circular cylinder at Reynolds numbers of 40 and 50. The main objective was to compare the obtained results with previous research and assess the agreement between them to validate the code STAR-CCM+.

Flow visualization techniques were employed to examine the flow patterns around the circular cylinder. The visualization revealed consistent patterns of flow separation, vortex shedding, and the formation of wake structures, all consistent with prior studies. This agreement confirms the reproducibility of these flow phenomena and supports the validity of the current investigation.

Additionally, the pressure distributions obtained along the surface of the circular cylinder closely matched the profiles documented in earlier research. Drag and lift coefficients were also similar to previous research and likewise with the Strouhal number.

Overall, this validation study successfully demonstrated that the flow characteristics over a circular cylinder at Reynolds number 40 and 50 were in good agreement with previous research. The consistent results across multiple parameters validate the code used in STAR-CCM+ to be reasonable in performing simulations on cylinders in a steady flow.

4 Preprocessing

Preprocessing in STAR-CCM+ is done inside the program to set up a simulation before running it. This is done by making a computational domain, applying a mesh and setting up boundary conditions, numerical models and turbulence. A description of this is presented in this chapter.

4.1 Computational Domain

The computational domain forms the foundation for CFD simulations, providing the spatial framework in which fluid flow phenomena are numerically analyzed. To accurately capture the behavior of flows and their interactions with surrounding structures, the computational domain must encompass a sufficient volume. By including the complete interaction region, the computational domain allows for a comprehensive understanding of flow physics and the resulting effects on structures [1].

Determining the optimal size of the computational domain is crucial, as both excessively large and insufficiently sized domains can compromise the accuracy and efficiency of simulations. On one hand, a domain that is too small may lead to truncated flow features, incomplete representation of boundary layers, and inaccurate predictions. On the other hand, an excessively large domain may introduce unnecessary computational costs and computational time without significant benefits.

The dimensions of the computational domain play a pivotal role in mitigating unwanted boundary effects. A sufficiently large computational domain helps minimize the influence of boundaries on the flow field, preventing artificial reflections or disturbances caused by boundary discontinuities. By maintaining an appropriate domain size, the simulation can focus on capturing the intrinsic flow behavior rather than being influenced by boundary artifacts.

The dimensions are also problem-dependent, with no universally applicable domain size suitable for all cases. Different flow phenomena, geometries, and boundary conditions necessitate specific considerations when defining the computational domain dimensions. Careful analysis of the physical problem at hand, along with knowledge of the expected flow behavior, guides the determination of an appropriate domain size that encapsulates the essential features of interest.

The computational domain used in this thesis is made after consulting with Fengjian Jiang at Sintef Ocean regarding length, width and depth. It is a three-dimensional cubic-shaped domain where the chosen size (X, Y, Z) is 65D · 30D · 10D. The center of the cylinder is 15D from the inlet boundary, 15D from the top and bottom boundary and 50D from the outlet. This is illustrated in Figure 15.
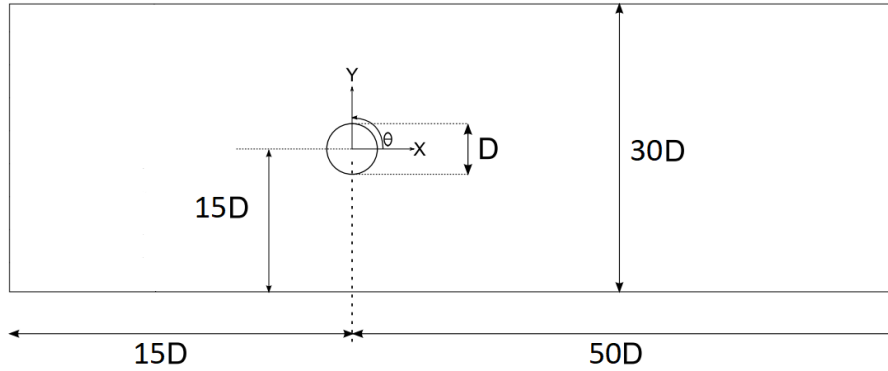
Figure 15: General setup of the computational domain used in the thesis.

This is a fairly large computational domain compared to other studies like Franke et al [19] which used a domain of the size (x, y, z) $30D \cdot 20D \cdot \pi D$.

4.2   Meshing

A powerful technique used in the STAR-CCM+ program to build high-quality computational meshes for various engineering simulations is structured meshing with refinements and a prism layer in the boundary layer. This method has a number of advantages, including accurate representation of complex geometries, improved solution convergence, and lower computational costs [1]. Below are a description on how the mesh is created.

The computational domain is initially partitioned equally into cubic cartesian grid boxes and a prism layer in the boundary layer. Furthermore, each grid box has NxNxN equal-sized cubic Cartesian grid cells that are dispersed uniformly. Normally, the biggest boxes are too coarse to capture information on complex flow phenomena, such as the shape of vortices. As a result, substantial grid refinement is required throughout the domain in the region where these complicated phenomena arise. A fine zonal grid is integrated into the global coarse grid in these regions. The smaller box is formed by evenly dividing all the coarse grid boxes into NxNxN tiny cubic Cartesian grid cells within the original grid box. As a result, the smaller boxes have a greater grid resolution that is roughly twice as fine as the larger ones. This grid refining process is carried out until the grid resolution is sufficient and the result is illustrated in Figure 16 where the boxes are getting smaller and smaller until the prism layer takes over. It is also worth mentioning that the refinement is stretched further downstream of the cylinder to capture the flow behind the cylinder.
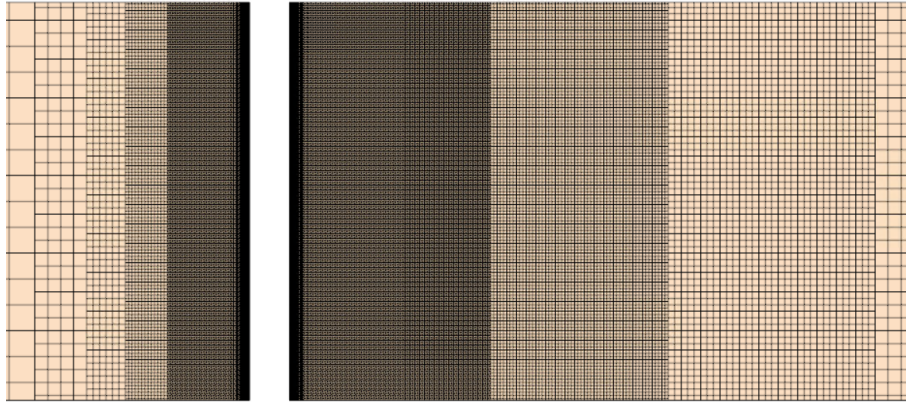
Figure 16: Illustration on how the mesh refinement works.

A prism layer is frequently used near solid surfaces in boundary layer simulations to accurately depict the flow behavior in this region. The prism layer is a thin layer of prismatic elements that extends from the surface of the structure throughout the boundary layer. This layer has a higher resolution and more properly captures the velocity and pressure gradients near the border. It is notably useful for capturing phenomena like viscous effects, heat transfer, and wall-bounded flows [1].

The prism layer in the current thesis follows the structured grid as the size of the prism layer cells is quite equal to the structured grid boxes in the beginning. Further, the cells get smaller and smaller closer to the cylinder to capture the viscous effect in the boundary layer as illustrated in Figure 17.
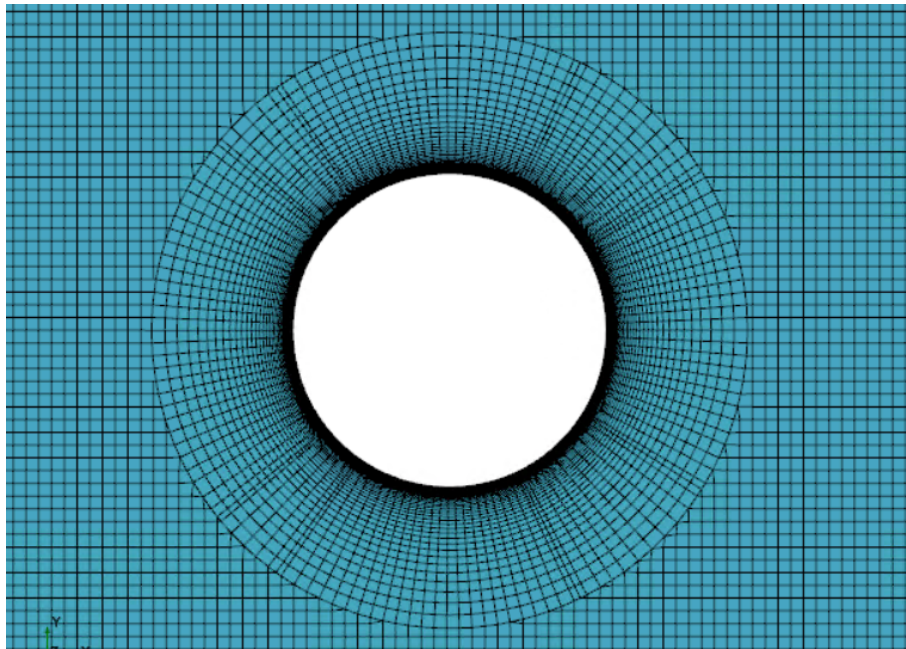

Figure 17: Illustration of prism layer in the boundary layer.

The geometry of the cylinder initially revealed certain oddities as it was discovered it wasn't completely circular, necessitating careful study during the meshing process. Three distinct simulations were run with increasing amounts of grid cells to test the sensitivity of the simulations to mesh resolution. A new cylinder model was constructed, however, to assure robustness and eliminate any errors caused by the previous geometry. Following that, three simulations were run on this revised cylinder, each with the same different number of grid cells. This method allows for a thorough examination of the effect of geometry on simulation results, allowing for more accurate findings and insights into the phenomena under investigation. Table 4 shows the mesh features used in the different simulations.

Table 4: Number of cells in the different grids used in simulations.

Cell numbers for different grids						
Geometry		Old			New	
Accuracy	Coarse	Medium	Fine	Coarse	Medium	Fine
Cells	2 662 116	10 361 818	18 631 382	2 538 220	8 210 932	19 550 976

4.2.1 Mesh Diagnostics

To determine the quality of the mesh, a thorough mesh diagnostics report was generated for each mesh generated in this thesis. The mesh diagnostics report was used to inspect the mesh for

- Mesh validity

- Face validity

- Volume change statistics

- Maximum interior skewness angle

- Maximum boundary skewness angle

The mesh validity check looks for unclosed cells, faulty cells or vertex references, zero face area cells, and cells with zero or negative volume. The face validity is an area-weighted measure of how accurate the face normals are in relation to their linked cell center. Volume change statistics describe the maximum and minimum ratios of a cell's volume to that of its closest neighbors. Cells having a volume change of 10^{-5} or less should be studied [1]. For all meshes, the mesh validity, face validity, and volume change statistics were all satisfactory.

In STAR-CCM+, skewness angles of 90 degrees or greater, which might occur in concave cells, are problematic. As a result, any skewness angle more than 85 degrees is not advised. The maximum skewness angle was kept under 50 degrees for all analyses.

According to CD Adapco [1], the aspect ratio of the cells in the mesh plays a role in simulations with LES. The point is that the cells should not be highly stretched.

This is a point worth mentioning as the cells in the boundary layer closest to the cylinder in this thesis are highly stretched.

4.3   Boundary conditions

Different parts of geometries have different physical properties, so they need different boundary conditions. This section gives a representation of the different boundary conditions used in STAR-CCM+ and in the simulations.

Velocity Inlet

The boundary condition *Velocity Inlet*, i.e. the inlet face velocity vector, is stated explicitly in STAR-CCM+. Using reconstruction gradients, the boundary face pressure is extrapolated from the next cell.

Pressure Outlet

Pressure Outlet states that the pressure on the outlet boundary must be zero. The boundary face velocity is extrapolated from the interior using reconstruction gradients at the pressure outlet.

Wall

The tangential velocity at the boundary is set to zero by employing this boundary condition. Using a reconstruction gradient, the boundary layer face pressure is extrapolated from neighboring cells. There will be no velocities through a wall-defined boundary.

Symmetry Plane

In STAR-CCM+, the shear stress in a Symmetry Plane is set to zero. The face value of the velocity is extrapolated from the parallel component of the velocity in the neighboring cell, as with the Pressure Outlet. The identical method is used to compute the boundary face pressure.

4.4   Physical models applied in STAR-CCM+

The physics module in STAR-CCM+ explains how a physical phenomenon in a continuum is represented. The physics modules establish the simulation's key variables such as velocity and pressure as well as the mathematical formulation required to obtain the answer. For the entire definition of a physics continuum, a mixture of models is required. The selected physics models in this thesis are the following:

- Time: Implicit Unsteady

- Space: Three Dimensional

- Material: Liquid

- Flow: Segregated Flow

- Equation of State: Constant Density

- Viscous Regime: Turbulent

- Turbulence: Large Eddy Simulations

- Subgrid Scale Turbulence: Dynamic Smagorinsky Subgrid Scale

- LES Wall Treatment: All y^+ Wall Treatment

4.5 Numerical Model

A «Figure of Eight» trajectory is assigned to the cylinder as field functions for the velocity and is the derivative of the following equations:

$$IL : x(t) = A_{IL} * sin(2\pi f_{osc,IL} * t + \alpha) \tag{25}$$

$$CF : y(t) = A_{CF} * cos(2\pi f_{osc,CF} * t) \tag{26}$$

The phase angle α in the IL-equation is used to control the orbital direction. In this thesis, only $\alpha = 0$ is considered and is illustrated in Figure 18.
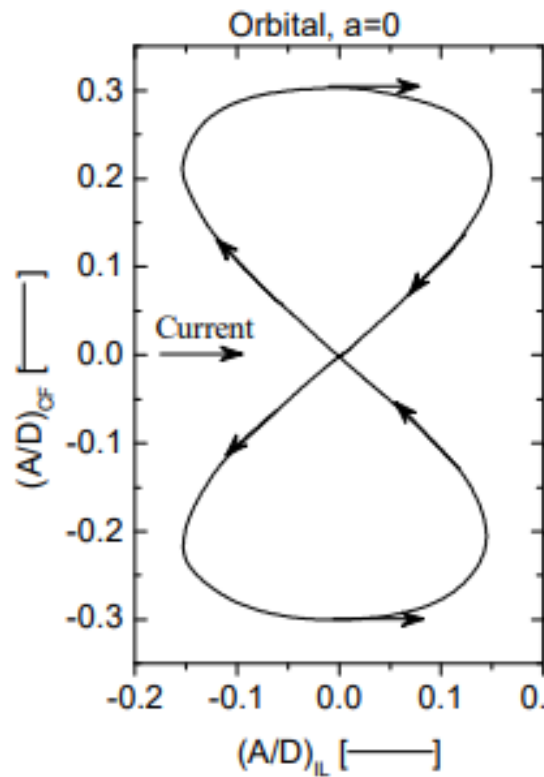

Figure 18: "Figure of eight" motion applied to the cylinder. Reprinted from Huang et al [48]

The characteristic parameters are identical to the ones used by Aronsen et al [4]:

$$f_{IL} = 0.325, f_{CF} = 0.1625, (A/D)_{IL} = 0.15, (A/D)_{CF} = 0.30 \qquad (27)$$

where the non-dimensional frequency is defined as $f_{IL,CF} = f_{osc,IL,CF} D/U_0$, where D is the diameter of the cylinder and U_0 is the incoming flow velocity.

4.6 Physical Parameters

The case describes a circular cylinder in infinite fluid with uniform flow. The case in question is three-dimensional, with Reynolds number of 24000, indicating that the flow regime is sub-critical. The diameter, D, is fixed at 0.1 m, the incoming flow has a fixed velocity of 0.24 m/s and the density is kept constant to 1000 kg/m^3 in the following study. In Table 5 all parameters are displayed.

Table 5: Physical parameters used in simulations.

Physical parameters				
U [m/s]	D [m]	ρ [kg/m^3]	μ [kg/ms]	Re [-]
0.24	0.1	1000	0.001	24000

5 Postprocessing

Different types of plots and scenes can be created with STAR-CCM+. The plots and scenes are created before starting the simulation and can be analyzed once the stopping condition is met and the simulation is completed. One can also consider the plots and scenes that appear during the simulation, which can be informative at first. This thesis also employed plots and scenes to determine when the flow was regarded as fully formed.

5.1 Scenes

The scenes in STAR-CCM+ are easily set up. Firstly a new scene is created and assigned to the wanted part before assigning the wanted field of view. The following scenes have been used to illustrate the graphical results in this thesis:

- Scalar scene for pressure contour lines

- Scalar scene for velocity contour lines

- Scalar scene for velocity components u and v

- Scalar scene for vorticity contour lines

- Scalar scene for convective courant number

- Scalar scene for streamlines around the cylinder

However, only vorticity contour lines and streamlines are presented in the thesis as seen in Figure 19 as the others are used to calculate coefficients or to look at the mesh diagnostics.
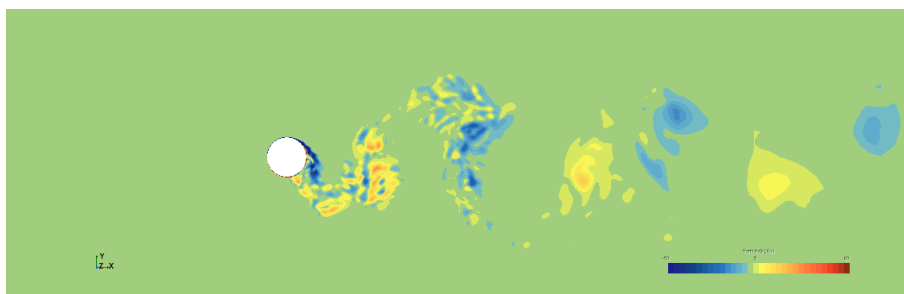

Figure 19: Illustration of vorticity behind the cylinder.

5.2 Plots

To make a plot in STAR-CCM+, you right-click the monitor option in the menu and select a new report. From there the wanted part is assigned with the wanted

statistics. By clicking create monitor and plot form report the statistics are presented in real time as the simulation is going. In this thesis the following plots have been generated in STAR-CCM+:

- Plot for F_D

- Plot for F_L

- Plot for pressure distribution around the cylinder surface

- Plot for the position of the cylinder in both the x and y direction

- Plot for the velocity of the cylinder in both the x and y direction

When the simulation is completed and the plots are finished they are easily exported to Matlab and they are illustrated as in Figure 20 where a plot of the residuals is presented.
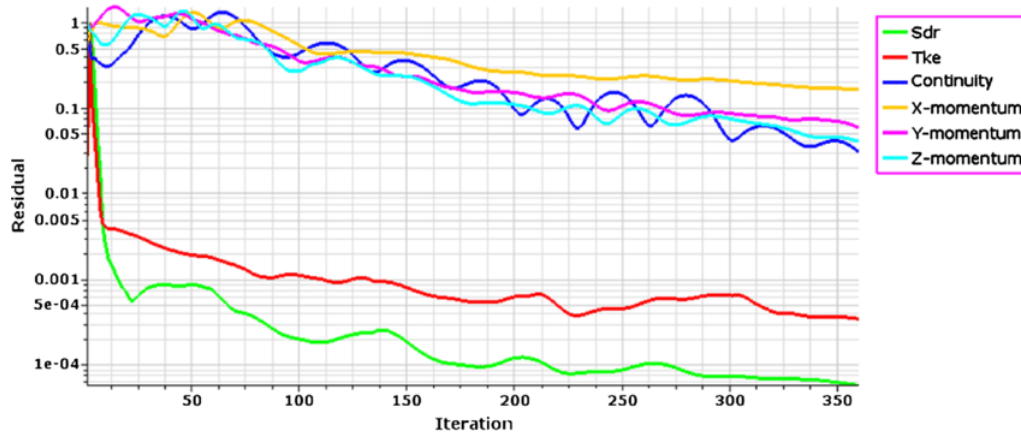

Figure 20: Illustration of a residuals plot in STAR-CCM+.

5.3   Matlab

All plots created in STAR-CCM+ are imported to Matlab for further analysis and calculation. The different calculations executed are:

- Time averaged drag coefficient C_D

- Time averaged RMS lift coefficient $C_{L,RMS}$

- Time averaged added mass coefficient C_a

- Time averaged excitation coefficient C_{lv}

- Pressure coefficient C_p over the cylinder surface

6 Results and Discussion

Although the geometry is basic, the round shape of the cylinder presents a barrier to numerical analyses. The separation points are not easily determined because of the absence of sharp edges. The placement is solely determined by the flow regime or the upstream conditions. As a result, numerical forecasts of turbulence statistics in the local region are particularly sensitive and can result in non-conformities.

In this chapter, the results are presented and discussed concerning the feasibility of the engineering method chosen in the thesis. This is done through verification of results and comparison with the previous studies done by Aronsen [4].

6.1 Figure of Eight Motion

The first thing to look at is the movement of the cylinder and how it moves according to the numerical model implemented on the cylinder. In Figure 23 the movement of the cylinder for one figure of eight period is presented. In the picture series, the cylinder moves right and left two times and up and down one time. This compares well with the implemented model as a closer look shows a clear figure of eight motion. The rheoretical motion in both x and y-direction is presented in Figure 21.
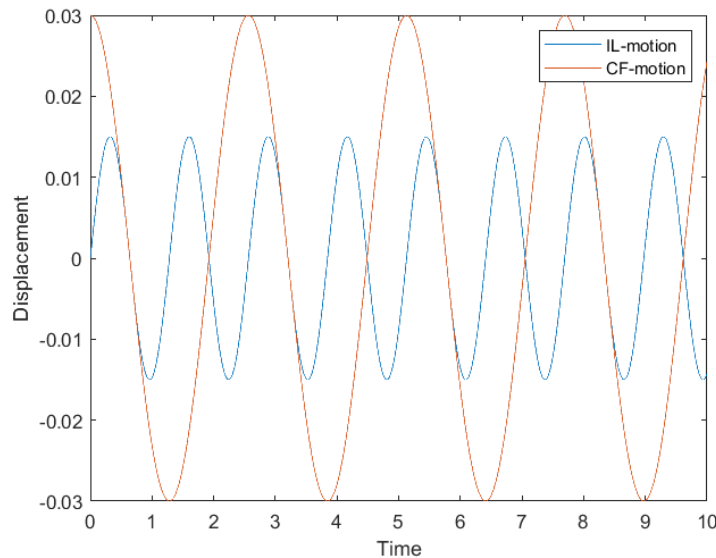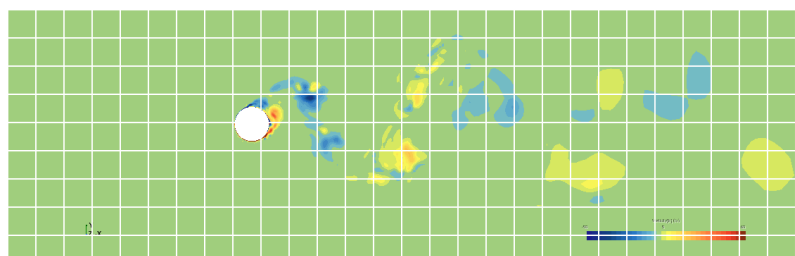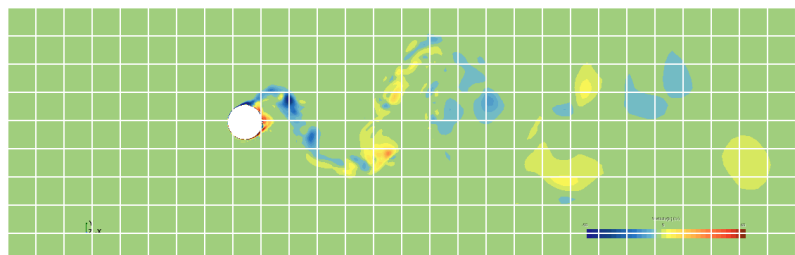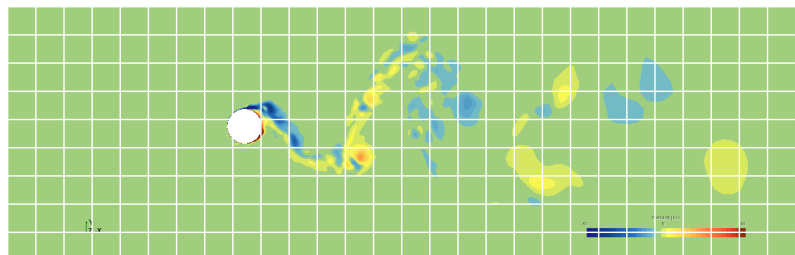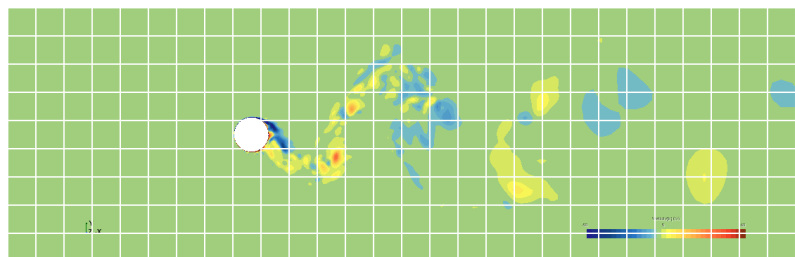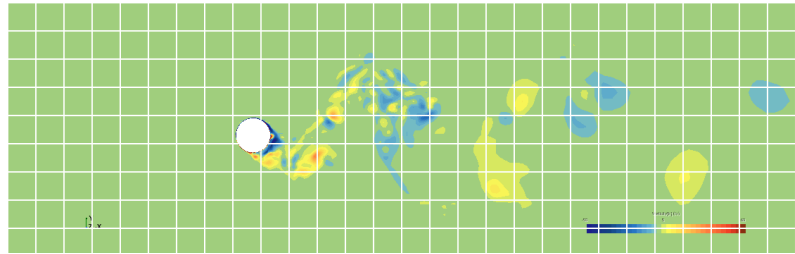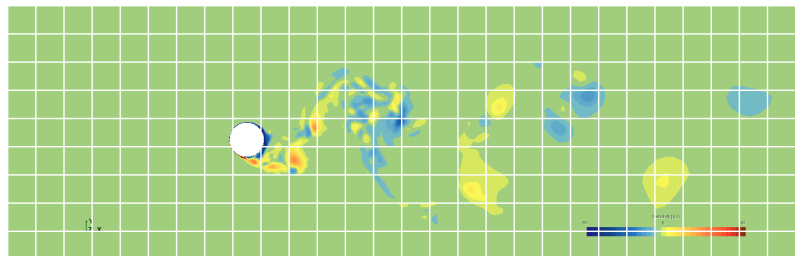

Figure 21: Theoretical motion in x and y direction of the cylinder
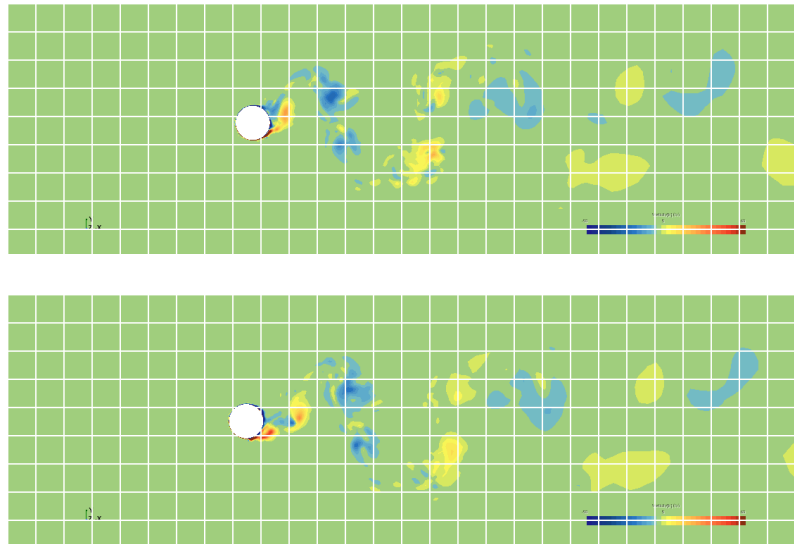
Figure 23: Motion of cylinder over one figure of eight period.

To verify the motion not only from the contour plots the cylinder was tracked during the simulations from an added point on the cylinder. This point moved with the cylinder and tracked its trajectory throughout the simulations and plotted them. These time series were later exported to Matlab where one period was plotted to verify the motion. This is presented in Figure 24 where the figure of eight motion is clear and compares exactly with the theoretical one from Huang [48] and Aronsen [4]. This was done for both the old and new mesh and came out the same. This proves that the applied motion was not a point of error in this thesis.

Figure 24: Calculated trajectory of the cylinder from Matlab.

6.2 Drag and Lift Forces

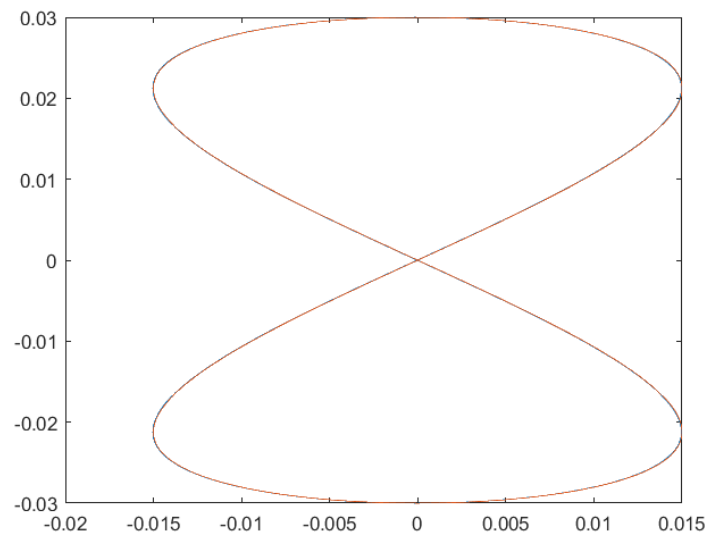The drag coefficient C_D and the RMS lift coefficient $C_{L,rms}$ are two often used performance metrics for evaluating the convergence of a mesh in a simulation. These factors provide useful information on the quality and stability of simulation findings, especially when dealing with fluid flow around objects. Therefore the plotted C_D and C_L are presented in Figure 25 to find discrepancies between the new and old mesh/geometry mentioned in Chapter 4 and at the same time look at the convergence.

A time averaged coefficients of drag and RMS lift is also a key point in looking at convergence for grids. This is presented in Table 6 and will be compared to the values from Aronsen's [4] experiments. A convergence plot for both coefficients is presented in Figure 26.

Table 6: Calculated drag and lift RMS coefficients for both grids for each simulation.

Number of cells [mill]	Old mesh		New mesh	
	C_D	$C_{L,rms}$	C_D	$C_{L,rms}$
2	1.578	2.071	1.662	1.535
8	1.835	2.308	1.779	1.632
18	1.703	1.963	1.601	1.451

From the time series of C_D and C_L in Figure 25 the differences from old to new mesh and different mesh sizes are plotted. This gives an understanding of what the discrepancy in the first geometry mentioned in the pre-processing chapter has on the results. The plots for the old grid are similar to each other and the same for the new grid as expected. The new mesh shows a rather more varying drag coefficient than the old mesh and the lift coefficient has a higher response in the old mesh than the new. This might be because of the tiny edges in the old mesh because of the circular geometry that did not come out as a complete circle.
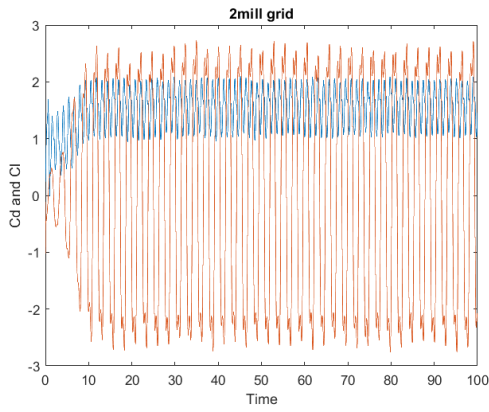
(a) Time series of drag and lift coefficient for the coarsest old mesh with 2 mill cells.
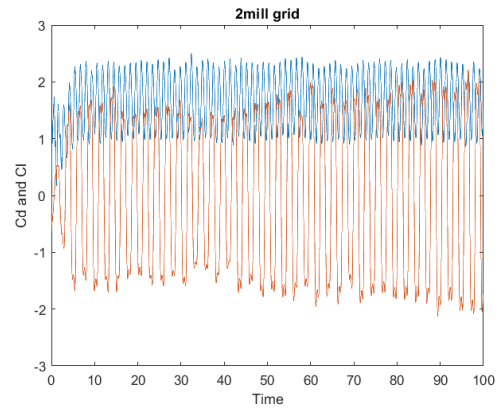
(b) Time series of drag and lift coefficient for the coarsest new mesh with 2 mill cells.
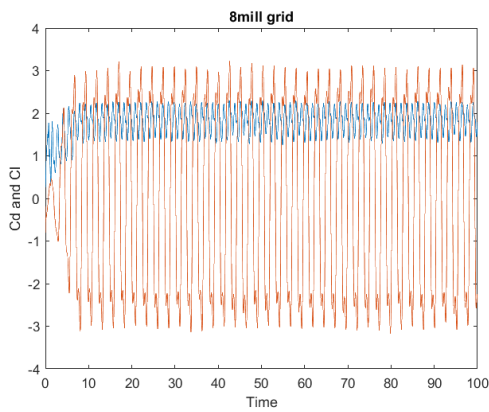
(c) Time series of drag and lift coefficient for the medium coarse old mesh with 8 mill cells.

(d) Time series of drag and lift coefficient for the medium coarse new mesh with 8 mill cells.

(e) Time series of drag and lift coefficient for the finest old mesh with 18 mill cells.

(f) Time series of drag and lift coefficient for the finest new mesh with 18 mill cells.

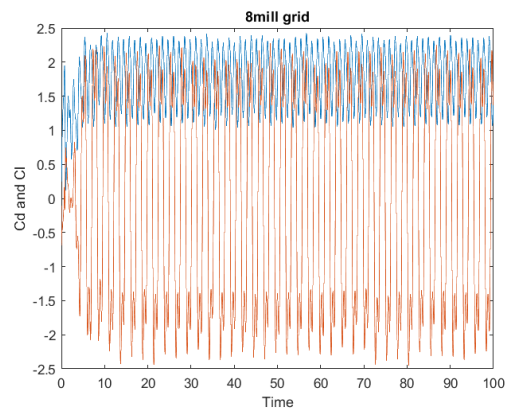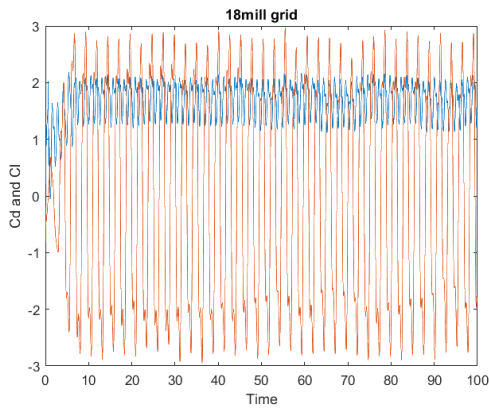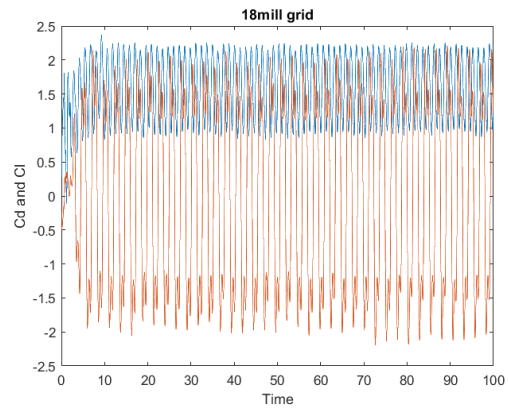Figure 25: Comparison of the new and old grids and how they differ from coarse to fine. Drag coefficient in blue and lift coefficient in red.

As mentioned previously C_D and $C_{L,rms}$ are performance metrics used for evaluating the convergence of a mesh in a simulation and provide useful information on the quality and stability of the mesh. In Figure 26 convergence plots for both coefficients are plotted for the old and new mesh. It is clear that the values do not converge at all. This is not only for the bad geometry of the first cylinder but for the new one as well. The inability to achieve mesh convergence shows that the existing mesh resolution and processing resources were insufficient to resolve the flow field's fine complexities. As a result, the hydrodynamic coefficients derived from simulation findings may be unreliable or unrepresentative of physical behavior.
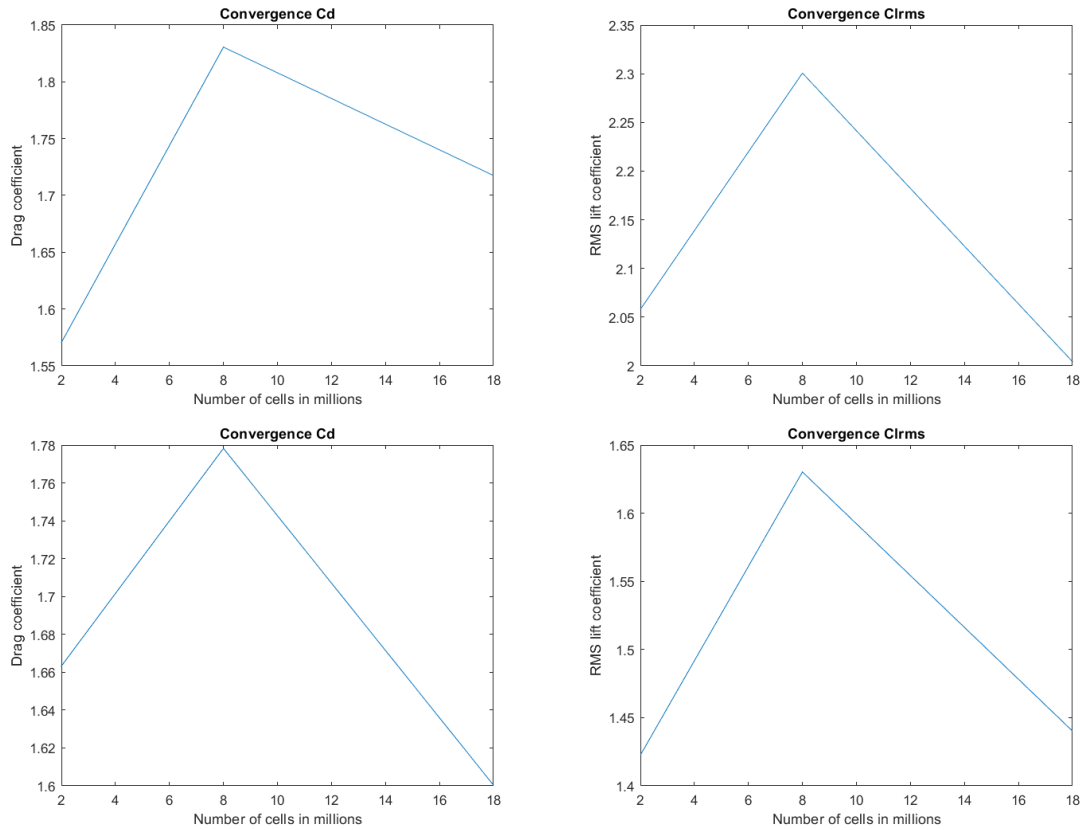
Figure 26: Convergence plots for C_D and $C_{L,rms}$ for the old (top) and new (bottom) mesh.

6.3   Added Mass and Excitation Coefficients

As the drag and RMS lift coefficients are raw force history there is a need for calculation of added mass and excitation coefficients to filter out the noises. These are presented in Tables 8 and 9 for both meshes and for the different numbers of cells. From these results, the IL values are the most similar to Aronsen's [4] results as they also were for the drag and lift coefficients. For the CF results, the values vary a lot more and values for the excitation coefficient are way off.

Table 7: Calculated hydrodynamic coefficients on port and starboard side of the cylinder from Aronsens studies.

	C_a		C_{lv}		C_D	$C_{L,rms}$
Direction	IL	CF	IL	CF	IL	CF
SB	-0.117	3.922	-0.193	-1.384	1.662	2.505
Port	-0.159	4.192	-0.209	-1.460	1.653	2.651

Table 8: Calculated in-line and cross-flow excitation coefficient C_{lv} for both the new and old mesh.

	Old mesh		New mesh	
Number of cells [mill]	IL	CF	IL	CF
2	-0.208	0.646	-0.333	-0.176
8	-0.154	1.152	-0.372	0.682
18	-0.333	1.780	-0.418	1.014

Table 9: Calculated in-line and cross-flow added mass coefficient C_a for both the new and old mesh.

	Old mesh		New mesh	
Number of cells [mill]	IL	CF	IL	CF
2	-0.226	3.082	-0.360	2.101
8	-0.189	3.385	-0.297	2.338
18	-0.163	2.842	-0.332	2.019

6.4   Sources of Error

As most experiments have sources of error also this one included some that may have affected the results.

The CFD-code must be implemented fairly in order to provide successful outcomes. In simple terms, the method should be applied to problems that it can accurately replicate.

Without a suitable mesh, the equations to be solved may not be adequately discretized in space. The mesh generation in this thesis is based on talks with Fengjian Jiang at Sintef Ocean and Prof Lars Erik Holmedal. The mesh is judged not resolved due to large variations in the mesh convergence study for both meshes in the thesis.

The discretization of the equations over time is determined by the time step. The magnitude of the time step employed in this thesis is determined after talks with supervisors. However, to ensure that the time step was small enough for the present use of the CFD code, a time step convergence study should be done. Due to time management limitations, this was not completed.

In the geometry modeler in STAR-CCM+ the geometry of a basic cylinder can go wrong as found in this thesis. This could have a significant effect on the results of

simulations and might be a problem for further work as it is hard to see when not looking for it. This could also be linked to human errors. They are always something to think about as a tired mind can make a lot of mistakes looking at a computer for a whole day.

6.5   Discussion

According to CD Adapco [1], the aspect ratio of the cells in the mesh plays a role in simulations with LES. The point is that the cells should not be highly stretched. This is a point worth mentioning as the cells in the boundary layer closest to the cylinder in this thesis are highly stretched. This is illustrated in Figure 27 where a close-up of the mesh close to the cylinder is presented. This may cause the boundary layer to not be fully resolved and might be the reason the results in CF-direction are so far of.
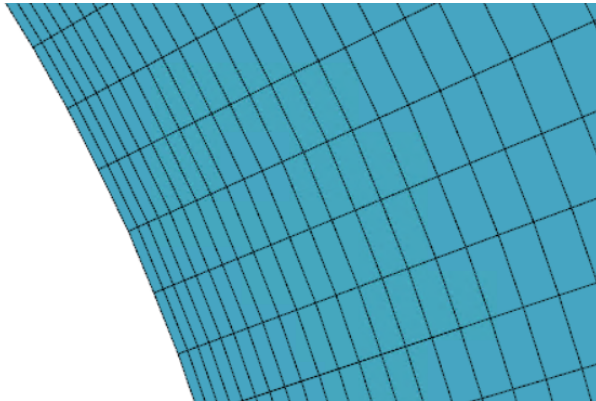

Figure 27: Close-up of the mesh close to the cylinder to show stretched cells.

From the results, the hydrodynamic coefficients are way off experimental values found by Aronsen [4]. This comes from either two things; the mesh is the wrong type to use in these simulations or the mesh is not fine enough. After talks with Prof. Lars Erik Holmedal, the solution to the thesis problem of developing an engineering model for this type of simulation in STAR-CCM+ was found to be either a new type of mesh or heavier and longer simulations with a finer mesh.

The implementation of the motion on the cylinder was successful and also the validation case. This gives an idea that the code could be used in problems like this but maybe with some other parameters such as the mesh.

All the hydrodynamic coefficients in the results are wrong compared to the experiments done by Aronsen [4]. This might be because of the simulation length. The simulations were run for 100 seconds real-time and this might not be enough as there is 40 CF periods in this time interval. This is the minimum according to Franke et al [19] and Lysenko et al [29] ran simulations for 150 periods. Note that these two cases were different from this regarding motion and Reynolds number but it is worth keeping in mind.

7   Conclusion

In this master thesis, the flow around a circular cylinder at Re = 24000 has been investigated using 3D LES. The aim was to develop an engineering method to numerically simulate a cylinder with forced oscillations like Aronsen [4] in the commercial code STAR-CCM+.

In the simulation, the forced motion was successfully applied. The cylinder was forced to oscillate in both the x and y directions, allowing the effects of forced motion on the turbulent flow around the cylinder to be studied.

The inability to achieve mesh convergence shows that the existing mesh resolution and processing resources were insufficient to resolve the flow field's fine intricacies. As a result, the hydrodynamic coefficients derived from simulation findings may be unreliable or unrepresentative of physical behavior.

Furthermore, the lack of successful comparison with earlier research impedes the simulation methodology's validation and verification. It is difficult to measure the correctness and authenticity of numerical data in the absence of a solid standard. This knowledge gap raises concerns about the simulation approach's predictive capability for similar marine applications employing circular cylinders.

Based on the data, it is possible to conclude that the simulation did not reach mesh convergence and that there was no successful comparison to earlier studies in terms of hydrodynamic coefficients and forced motion. The mesh type and size, as well as the mesh time given, were insufficient for accurately capturing the turbulent 3D flow around the oscillating cylinder.

8   Further work

Free stream flow over a circular cylinder with forced motion is not a basis for many numerical investigations. It is a complex problem with a number of possible errors. The work done in this thesis was troubled with problems from the start regarding geometry and meshing in STAR-CCM+, but with the problems in mind a good starting point for developing a working numerical model. Here are some suggestions to further work.

Heavier simulations. The work done in this thesis is computationally simple when using a supercomputer and a solution can be to make the mesh much finer and run longer simulations and in doing so, resolve the boundary layer better. This method can work but will take a larger amount of time on meshing and simulations.

New type of mesh. In order to resolve the boundary layer better a new type of mesh could be used where the aspect ratio of the cells is much lower than in the mesh used in this thesis.

Simplify the problem. As this problem is very complex having forced motion in both x and y-direction a solution could be to start with only cross-flow oscillations making the simulations easier. Then do the same with only in-line oscillations and develop the model further from there.

Bibliography

[1] CD-Adapco. *Star-CCM+ User Guide*. 2016.

[2] P. Anagnostopoulos and P.W. Bearman. 'Response characteristics of a vortex-excited cylinder at low reynolds numbers'. In: *Journal of Fluids and Structures* 6.1 (1992), pp. 39–50. ISSN: 0889-9746. DOI: https://doi.org/10.1016/0889-9746(92)90054-7. URL: https://www.sciencedirect.com/science/article/pii/0889974692900547.

[3] Dale A Anderson. *Computational fluid mechanics and heat transfer*. eng. Boca Raton, Fla, 2021.

[4] Kristoffer Aronsen. 'An Experimental Investigation of In-line and Combined In-line and Cross-flow Vortex Induced Vibrations'. In: (Jan. 2007).

[5] B. Pettersen. *Numerical Methods in Marine Hydrodynamics - Lecture Notes*. Department Of Marine Technology, NTNU, Trondheim. 2019.

[6] G.S. Baarholm, C.M. Larsen and H. Lie. 'On fatigue damage accumulation from in-line and cross-flow vortex-induced vibrations on risers'. In: *Journal of Fluids and Structures* 22.1 (2006), pp. 109–127. ISSN: 0889-9746. DOI: https://doi.org/10.1016/j.jfluidstructs.2005.07.013. URL: https://www.sciencedirect.com/science/article/pii/S0889974605001234.

[7] Dong-Geun Baek et al. 'Effects of the advance ratio on the evolution of a propeller wake'. In: *Computers Fluids* 118 (2015), pp. 32–43. ISSN: 0045-7930. DOI: https://doi.org/10.1016/j.compfluid.2015.06.010. URL: https://www.sciencedirect.com/science/article/pii/S0045793015001930.

[8] Hugh Blackburn and Ron Henderson. 'Lock-in behavior in simulated vortex-induced vibration'. In: *Experimental Thermal and Fluid Science* 12.2 (1996), pp. 184–189. ISSN: 0894-1777. DOI: https://doi.org/10.1016/0894-1777(95)00093-3. URL: https://www.sciencedirect.com/science/article/pii/0894177795000933.

[9] Tian Cai et al. 'Numerical investigation of flow around a step cylinder'. In: May 2017.

[10] J. CARBERRY, J. SHERIDAN and D. ROCKWELL. 'Controlled oscillations of a cylinder: forces and wake modes'. In: *Journal of Fluid Mechanics* 538 (2005), pp. 31–69. DOI: 10.1017/S0022112005005197.

[11] Yunus Cengel and John Cimbala. *EBOOK: Fluid Mechanics Fundamentals and Applications (SI units)*. McGraw Hill, 2013.

[12] H.C Chen, V.C Patel and S Ju. 'Solutions of Reynolds-averaged Navier-Stokes equations for three-dimensional incompressible flows'. In: *Journal of Computational Physics* 88.2 (1990), pp. 305–336. ISSN: 0021-9991. DOI: https://doi.org/10.1016/0021-9991(90)90182-Z. URL: https://www.sciencedirect.com/science/article/pii/002199919090182Z.

[13] E. Constant et al. 'An immersed boundary method in OpenFOAM : Verification and validation'. In: *Computers Fluids* 157 (2017), pp. 55–72. ISSN: 0045-7930. DOI: https://doi.org/10.1016/j.compfluid.2017.08.001. URL: https://www.sciencedirect.com/science/article/pii/S004579301730275X.

[14]   Veritas D. N. 'Recommended Practice: Free spanning pipelines'. In: *DNVGL-RP-F105* (July 2017).

[15]   S. C. R. Dennis and Gau-Zu Chang. 'Numerical solutions for steady flow past a circular cylinder at Reynolds numbers up to 100'. In: *Journal of Fluid Mechanics* 42.3 (1970), pp. 471–489. DOI: 10.1017/S0022112070001428.

[16]   J. Donea, S. Giuliani and J.P. Halleux. 'An arbitrary lagrangian-eulerian finite element method for transient dynamic fluid-structure interactions'. In: *Computer Methods in Applied Mechanics and Engineering* 33.1 (1982), pp. 689–723. ISSN: 0045-7825. DOI: https://doi.org/10.1016/0045-7825(82)90128-1. URL: https://www.sciencedirect.com/science/article/pii/0045782582901281.

[17]   Joel H Ferziger, Milovan Perić and Robert L Street. *Computational methods for fluid dynamics*. Vol. 3. Springer, 2002.

[18]   Bengt Fornberg. 'A numerical study of steady viscous flow past a circular cylinder'. In: *Journal of Fluid Mechanics* 98.4 (1980), pp. 819–855. DOI: 10.1017/S0022112080000419.

[19]   J. Franke and W. Frank. 'Large eddy simulation of the flow past a circular cylinder at ReD=3900'. In: *Journal of Wind Engineering and Industrial Aerodynamics* 90.10 (2002). 3rd European-African Conference on Wind Engineering, pp. 1191–1206. ISSN: 0167-6105. DOI: https://doi.org/10.1016/S0167-6105(02)00232-5. URL: https://www.sciencedirect.com/science/article/pii/S0167610502002325.

[20]   Jorgen Fredsoe and B Mutlu Sumer. *Hydrodynamics Around Cylindrical Structures (Revised Edition)*. eng. Singapore: World Scientific Publishing Company, 2006. ISBN: 9789812700391.

[21]   J. H. Gerrard. 'The mechanics of the formation region of vortices behind bluff bodies'. In: *Journal of Fluid Mechanics* 25.2 (1966), pp. 401–413. DOI: 10.1017/S0022112066001721.

[22]   R. GOVARDHAN and C. H. K. WILLIAMSON. 'Resonance forever: existence of a critical mass and an infinite regime of resonance in vortex-induced vibration'. In: *Journal of Fluid Mechanics* 473 (2002), pp. 147–166. DOI: 10.1017/S0022112002002318.

[23]   A. S. Grove, F. H. Shair and E. E. Petersen. 'An experimental investigation of the steady separated flow past a circular cylinder'. In: *Journal of Fluid Mechanics* 19.1 (1964), pp. 60–80. DOI: 10.1017/S0022112064000544.

[24]   Xiaoyi He and Gary Doolen. 'Lattice Boltzmann Method on Curvilinear Coordinates System: Flow around a Circular Cylinder'. In: *Journal of Computational Physics* 134.2 (1997), pp. 306–315. ISSN: 0021-9991. DOI: https://doi.org/10.1006/jcph.1997.5709. URL: https://www.sciencedirect.com/science/article/pii/S0021999197957090.

[25]   Howard H. Hu, N.A. Patankar and M.Y. Zhu. 'Direct Numerical Simulations of Fluid–Solid Systems Using the Arbitrary Lagrangian–Eulerian Technique'. In: *Journal of Computational Physics* 169.2 (2001), pp. 427–462. ISSN: 0021-9991. DOI: https://doi.org/10.1006/jcph.2000.6592. URL: https://www.sciencedirect.com/science/article/pii/S0021999100965926.

[26] H. Al-Jamal and C. Dalton. 'Vortex induced vibrations using Large Eddy Simulation at a moderate Reynolds number'. In: *Journal of Fluids and Structures* 19.1 (2004), pp. 73–92. ISSN: 0889-9746. DOI: https://doi.org/10.1016/j.jfluidstructs.2003.10.005. URL: https://www.sciencedirect.com/science/article/pii/S0889974603001786.

[27] N. JAUVTIS and C. H. K. WILLIAMSON. 'The effect of two degrees of freedom on vortex-induced vibration at low mass and damping'. In: *Journal of Fluid Mechanics* 509 (2004), pp. 23–62. DOI: 10.1017/S0022112004008778.

[28] D. JEON and M. GHARIB. 'ON CIRCULAR CYLINDERS UNDERGOING TWO-DEGREE-OF-FREEDOM FORCED MOTIONS'. In: *Journal of Fluids and Structures* 15.3 (2001), pp. 533–541. ISSN: 0889-9746. DOI: https://doi.org/10.1006/jfls.2000.0365. URL: https://www.sciencedirect.com/science/article/pii/S0889974600903657.

[29] Dmitry Lysenko, Ivar Ertesvåg and Kjell Erik Rian. 'Large-Eddy Simulation of the Flow Over a Circular Cylinder at Reynolds Number 3900 Using the OpenFOAM Toolbox'. In: *Flow, Turbulence and Combustion* 89 (Dec. 2012). DOI: 10.1007/s10494-012-9405-0.

[30] M. Greco. *Sea Loads - Lecture Notes.* Department Of Marine Technology, NTNU, Trondheim. 2021.

[31] G. Moe and Z.-J. Wu. 'The Lift Force on a Cylinder Vibrating in a Current'. In: *Journal of Offshore Mechanics and Arctic Engineering* 112.4 (Nov. 1990), pp. 297–303. ISSN: 0892-7219. DOI: 10.1115/1.2919870. eprint: https://asmedigitalcollection.asme.org/offshoremechanics/article-pdf/112/4/297/5579982/297_1.pdf. URL: https://doi.org/10.1115/1.2919870.

[32] J. Wu P. e. Voie C. M. Larsen and T. Resvanis. *VIV Best Practice: Guideline on analysis of vortex-induced vibrations in risers and umbilicals.* Tech. rep. 18SPIUB-18. 1322 Høvik: Det Norske Veritas AS, Sept. 2016.

[33] P. Spalart, W. Jou, M. Strelets and S. Allmaras. *"Comments on the Feasibility of LES for Wings and on the Hybrid RANS/LES approach". Advances in DNS/LES, Proceedings of the First AFOSR International Conference on DNS/LES.* 1997.

[34] Jack Park, Daniel Linton and Ben Thornber. 'Towards DES of Flow Around a Rotorcraft Fuselage Using an Immersed Boundary Method'. In: (Dec. 2019).

[35] Nikolaus Peller et al. 'High-order stable interpolations for immersed boundary methods'. In: *International Journal for Numerical Methods in Fluids* 52 (Dec. 2006), pp. 1175–1193. DOI: 10.1002/fld.1227.

[36] Lixia Qu et al. 'Quantitative numerical analysis of flow past a circular cylinder at Reynolds number between 50 and 200'. In: *Journal of Fluids and Structures* 39 (2013), pp. 347–370. ISSN: 0889-9746. DOI: https://doi.org/10.1016/j.jfluidstructs.2013.02.007. URL: https://www.sciencedirect.com/science/article/pii/S0889974613000388.

[37] Filippo Salmoiraghi, Angela Scardigli and Haysam Telib. 'Free Form Deformation, mesh morphing and reduced order methods: enablers for efficient aerodynamic shape optimization'. In: *International Journal of Computational Fluid Dynamics* 32 (Mar. 2018). DOI: 10.1080/10618562.2018.1514115.

[38] T. Sarpkaya. 'Hydrodynamic Damping, Flow-Induced Oscillations, and Biharmonic Response'. In: *Journal of Offshore Mechanics and Arctic Engineering* 117.4 (Nov. 1995), pp. 232–238. ISSN: 0892-7219. DOI: 10.1115/1.2827228. eprint: https://asmedigitalcollection.asme.org/offshoremechanics/article-pdf/117/4/232/5534644/232_1.pdf. URL: https://doi.org/10.1115/1.2827228.

[39] Günter Schewe. 'On the force fluctuations acting on a circular cylinder in crossflow from subcritical up to transcritical Reynolds number'. In: *Journal of Fluid Mechanics* 133 (Aug. 1983), pp. 265–285. DOI: 10.1017/S0022112083001913.

[40] Sintef. *Vortex-Induced Vibrations (VIV): fundamental concepts*. 2022.

[41] Owen Staten, Salinger Shontz and Coffey. *A Comparison of Mesh Morphing Methods for 3D Shape Optimization*.

[42] M. S. Triantafyllou et al. 'Vortex-Induced Vibrations of Slender Structures in Shear Flow'. In: *IUTAM Symposium on Integrated Modeling of Fully Coupled Fluid Structure Interactions Using Analysis, Computations and Experiments*. Ed. by Haym Benaroya and Timothy J. Wei. Dordrecht: Springer Netherlands, 2003, pp. 313–327. ISBN: 978-94-007-0995-9.

[43] D. J. Tritton. 'Experiments on the flow past a circular cylinder at low Reynolds numbers'. In: *Journal of Fluid Mechanics* 6.4 (1959), pp. 547–567. DOI: 10.1017/S0022112059000829.

[44] Mustafa Tutar and Arne E. Holdo. 'Large Eddy Simulation of a Smooth Circular Cylinder Oscillating Normal to a Uniform Flow '. In: *Journal of Fluids Engineering* 122.4 (May 2000), pp. 694–702. ISSN: 0098-2202. DOI: 10.1115/1.1287270. eprint: https://asmedigitalcollection.asme.org/fluidsengineering/article-pdf/122/4/694/5615335/694_1.pdf. URL: https://doi.org/10.1115/1.1287270.

[45] K. VIKESTAD, J.K. VANDIVER and C.M. LARSEN. 'ADDED MASS AND OSCILLATION FREQUENCY FOR A CIRCULAR CYLINDER SUBJECTED TO VORTEX-INDUCED VIBRATIONS AND EXTERNAL DISTURBANCE'. In: *Journal of Fluids and Structures* 14.7 (2000), pp. 1071–1088. ISSN: 0889-9746. DOI: https://doi.org/10.1006/jfls.2000.0308. URL: https://www.sciencedirect.com/science/article/pii/S0889974600903086.

[46] David C. Wilcox. *Turbulence modelling for CFD*. Third. DCW Industries, 2006.

[47] T. Ye et al. 'An Accurate Cartesian Grid Method for Viscous Incompressible Flows with Complex Immersed Boundaries'. In: *Journal of Computational Physics* 156.2 (1999), pp. 209–240. ISSN: 0021-9991. DOI: https://doi.org/10.1006/jcph.1999.6356. URL: https://www.sciencedirect.com/science/article/pii/S0021999199963568.

[48] C.M Larsen Z.Y Huang and W.C Cui. '3-D LES STUDY ON A FORCED OSCILLATING CIRCULAR CYLINDER FOLLOWING THE FIGURE OF EIGHT MOVEMENT'. In: (2009). ISSN: 0894-1777.

[49] Ming Zhao. 'Numerical simulation of vortex-induced vibration of a circular cylinder in a spanwise shear flow'. In: *Physics of Fluids* 27 (June 2015), p. 063101. DOI: 10.1063/1.4921882.